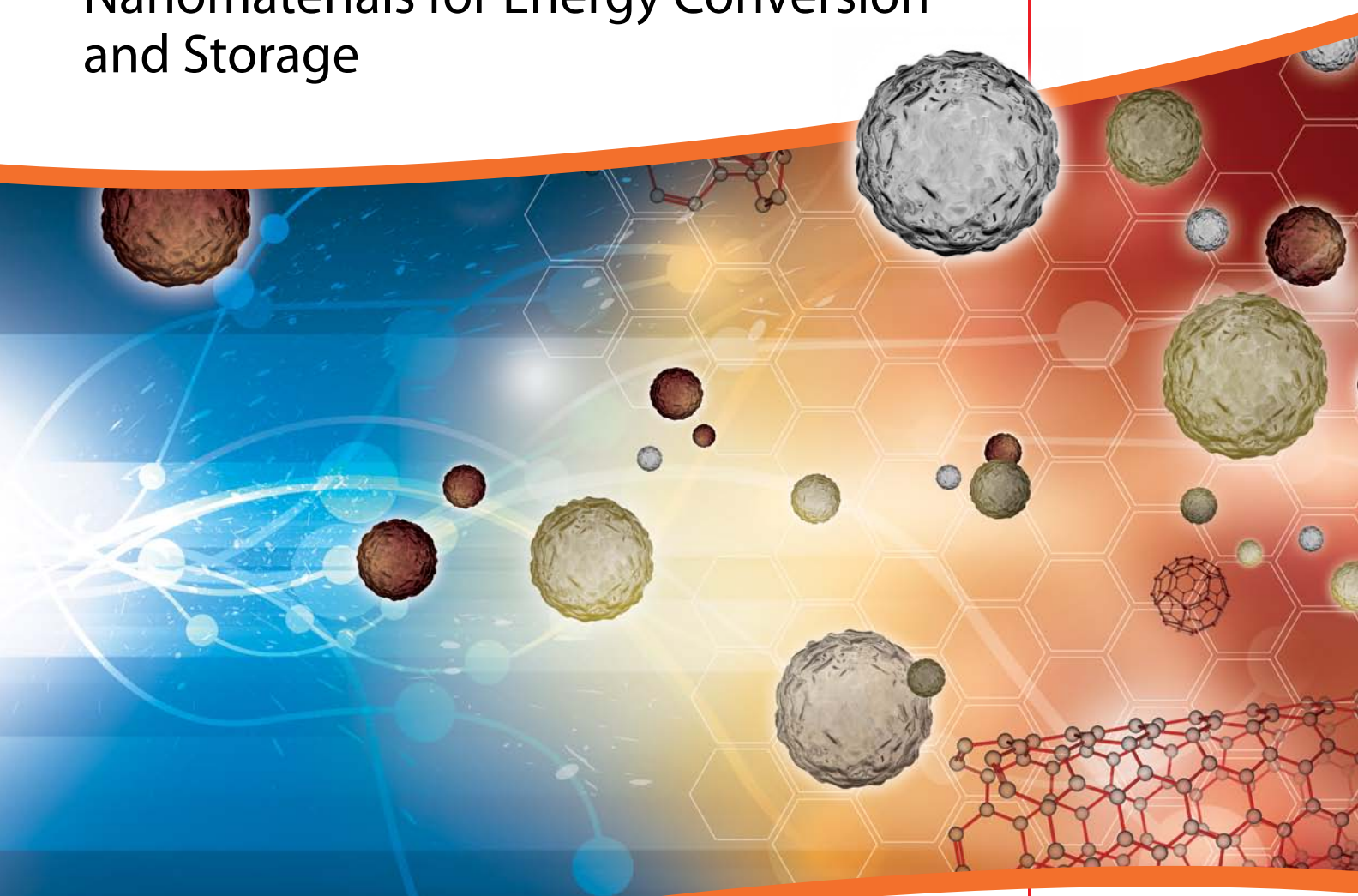


# Material Matters™

Volume 7, Number 4

**ALDRICH**  
Materials Science

## Nanomaterials for Energy Conversion and Storage



*Technologies for a changing world*

Electrode Materials for Lithium Ion Batteries

Surface-enhanced Solar Energy Conversion Systems Using Gold and Silver Nanoparticles

Materials for Clean H<sub>2</sub> Production from Bioethanol Reforming

Changing the Landscape of Environmental and Energy Research Through Novel Nanoscale Materials

**SIGMA-ALDRICH®**

## Introduction

Welcome to the fourth issue of *Material Matters*™ for 2012 focusing on Nanomaterials for Energy Conversion and Storage. The dual challenges of energy conversion and storage are pivotal to economic growth in the 21<sup>st</sup> century as technology rises to face new economic and environmental challenges. While fossil fuels have powered economic progress since the industrial revolution, the long-term environmental effects and finite supply of these energy sources require the transition to new, cleaner technologies. In addition, the increasing demand for energy created by a rising global standard of living, expected to reach at least 28 terawatts by 2050, creates a further need for the expansion and improvement of alternative energy technologies.

In order to tackle future energy challenges, alternative power sources must accomplish two goals. First, these materials must overcome the price and efficiency challenges that have so far prevented their use as a primary source of electricity. Second, since the majority of alternative energy technologies rely on intermittent power sources such as solar or wind, better energy storage technologies must be created to allow access to energy 24 hours a day. One promising general approach to meeting both of these challenges is improved efficiency through the application of nanoscale materials.

Nanomaterials, those with at least one dimension less than 100 nm, are a class of materials of great interest due to their enhanced size-dependent properties. These properties can take the form of unique electronic or optical characteristics, as well as enhanced surface area and reactivity. Such novel and improved properties make nanoscale materials promising candidates for improvements in alternative energy, either through the creation of new technology or the enhancement of existing systems. Our current issue presents articles from four leading scientists discussing the impact of nanomaterials on the future of alternative energy conversion and storage.

In our first article, Professor Marca Doeff (Lawrence Berkeley National Laboratory, USA) addresses the current state of lithium ion battery materials and the use of nanomaterials to improve their performance. This article highlights the challenges of balancing performance, lifetime and safety in lithium ion batteries, and the ways in which nanomaterials can both improve device performance while mitigating disadvantageous material attributes.

In the second article, Professors Shanlin Pan and Arunava Gupta (University of Alabama, USA), address the potential of plasmonic nanoparticles to enhance solar energy conversion. Surface plasmon resonance occurs on the surface of metallic nanoparticles and can enhance the performance of photovoltaic and photocatalytic systems by improving light absorption. As discussed in this review, such systems using gold or silver nanoparticles can significantly contribute to solar cell efficiency.

In the third article, Professors Kenneth Poepelmeier and Eric Weitz (Northwestern University, USA) discuss the use of nanoscale-supported metal clusters in the steam reforming of bioethanol to produce hydrogen. Hydrogen remains a promising clean fuel and an essential industrial material where the finite supply of fossil fuels is causing a shift to renewable feedstocks. While the factors dictating performance are addressed for hydrogen generation from ethanol, the importance of metal, support, promoter and preparation technique are universally relevant to heterogeneous systems.

In the final article, Professor Santanu Chaudhuri (Washington State University, USA) reviews the relationship between computational modeling and experiment in the search for nanoscale materials for clean energy. Nanoscale materials bridge the gap between single-site and supported systems and are essential to addressing the future of energy efficiency in applications ranging from emission reduction to hydrogen fuel cells. In order to address new energy challenges, a full understanding of the relationship between electronic structure and performance is required to reliably predict real-world properties of theoretical materials.

Each article in this publication is accompanied by a list of relevant materials available from Aldrich® Materials Science. For additional product information, visit Aldrich Materials Science at [aldrich.com/matsci](http://aldrich.com/matsci). Send us your comments or suggestions for *Material Matters*™ or your product suggestions to [matsci@sial.com](mailto:matsci@sial.com).

## About Our Cover

Among the most important technological challenges being addressed by nanotechnology are energy conversion and storage. New nanostructured materials for batteries (p. 56), photovoltaics (p. 64), and catalysts (pp. 70 and 76) are essential to addressing 21<sup>st</sup> century energy demands. The cover art of this issue represents the conversion and storage of energy using nanomaterials, which are crucial components of alternative energy-related technologies.



Adam Raw, Ph.D.  
Aldrich Materials Science  
Sigma-Aldrich Co. LLC

## Material Matters™

Vol. 7, No. 4

**Aldrich Materials Science  
Sigma-Aldrich Co. LLC**  
6000 N. Teutonia Ave.  
Milwaukee, WI 53209, USA

### To Place Orders

Telephone 800-325-3010 (USA)  
FAX 800-325-5052 (USA)

International customers, contact your local Sigma-Aldrich office ([sigma-aldrich.com/worldwide-offices](http://sigma-aldrich.com/worldwide-offices)).

### Customer & Technical Services

Customer Inquiries	800-325-3010
Technical Service	800-231-8327
SAFC®	800-244-1173
Custom Synthesis	800-244-1173
Flavors & Fragrances	800-227-4563
International	314-771-5765
24-Hour Emergency	314-776-6555
Safety Information	<a href="http://sigma-aldrich.com/safetycenter">sigma-aldrich.com/safetycenter</a>
Website	<a href="http://sigma-aldrich.com">sigma-aldrich.com</a>
Email	<a href="mailto:aldrich@sial.com">aldrich@sial.com</a>

### Subscriptions

Request your FREE subscription to *Material Matters*:

Phone	800-325-3010 (USA)
Mail	Attn: Marketing Communications Aldrich Chemical Co., Inc Sigma-Aldrich Co. LLC P.O. Box 2988 Milwaukee, WI 53201-2988
Website	<a href="http://aldrich.com/mm">aldrich.com/mm</a>
Email	<a href="mailto:sams-usa@sial.com">sams-usa@sial.com</a>

*Material Matters* (ISSN 1933-9631) is a publication of Aldrich Chemical Co., Inc. Aldrich is a member of the Sigma-Aldrich Group.

### Online Versions



Explore previous editions of  
*Material Matters*. Visit  
[aldrich.com/materialmatters](http://aldrich.com/materialmatters)

©2012 Sigma-Aldrich Co. LLC. All rights reserved.  
SIGMA, SAFC, SIGMA-ALDRICH, ALDRICH, and SUPELCO are trademarks of Sigma-Aldrich Co. LLC, registered in the US and other countries. FLUKA is a trademark of Sigma-Aldrich GmbH, registered in the US and other countries. Material Matters and Lumidot are trademarks of Sigma-Aldrich Co. LLC. Sigma brand products are sold through Sigma-Aldrich, Inc. Purchaser must determine the suitability of the product(s) for their particular use. Additional terms and conditions may apply. Please see product information on the Sigma-Aldrich website at [www.sigmaaldrich.com](http://www.sigmaaldrich.com) and/or on the reverse side of the invoice or packing slip.

# Table of Contents

## Articles

Electrode Materials for Lithium Ion Batteries . . . . .	56
Surface-enhanced Solar Energy Conversion Systems Using Gold and Silver Nanoparticles . . . . .	64
Materials for Clean H <sub>2</sub> Production from Bioethanol Reforming . . . . .	70
Changing the Landscape of Environmental and Energy Research Through Novel Nanoscale Materials . . . . .	76

## Featured Products

Electrode Sheets . . . . .	61
<i>(Electrode sheets for battery fabrication)</i>	
Cathode Materials . . . . .	61
<i>(A list of cathode materials for battery applications)</i>	
Anode Materials: Lithium, Titanate and Tin . . . . .	61
<i>(A selection of lithium and tin anode materials for batteries)</i>	
Anode Materials: Carbon and Silicon . . . . .	62
<i>(A list of carbon and silicon materials for battery anodes)</i>	
Electrolyte Materials . . . . .	62
<i>(A selection of materials for battery electrolytes)</i>	
Solvents and Additives . . . . .	62
<i>(A selection of solvents for use in battery applications)</i>	
Iron(III) Oxide (Fe <sub>2</sub> O <sub>3</sub> ) Materials . . . . .	67
<i>(A list of iron oxide materials for use in water splitting photocatalysis)</i>	
Silver Nanoparticles . . . . .	67
<i>(A list of silver nanoparticles for use in photonics)</i>	
One-dimensional Gold Nanostructures Stabilized in CTAB . . . . .	68
<i>(A selection of one-dimensional gold particles for use in photonics)</i>	
Gold Nanoparticles Stabilized in Citrate . . . . .	68
<i>(A list of gold nanoparticles for use in photonics)</i>	
Nanoscale Catalyst Supports . . . . .	73
<i>(A list of nanoscale oxide suitable for use as catalyst supports)</i>	
Ruthenium Catalysis Precursors . . . . .	74
<i>(A selection of precursors for ruthenium catalyst preparation)</i>	
Supported Ruthenium Catalysts . . . . .	74
<i>(A list of supported ruthenium catalysts)</i>	
Noble Metal Catalysts . . . . .	80
<i>(A selection of noble metal particles for use in catalysis)</i>	
Noble Metal Precursors . . . . .	81
<i>(A list of precursors for noble metal catalyst preparation)</i>	
Catalyst Supports . . . . .	81
<i>(A selection of materials suitable for use as catalyst supports)</i>	

# Your Materials Matter



*Shashi Jasty*

Shashi G. Jasty, Ph.D.  
Director, Aldrich Materials Science

We welcome fresh product ideas from you. Do you have a material or compound you wish to see in our Aldrich® Materials Science line? If it is needed to accelerate your research, it matters. Send your suggestion to [matsci@sial.com](mailto:matsci@sial.com) for consideration.

Professor Mercuri Kanatzidis of Northwestern University, Evanston, Illinois, USA, suggested the addition of high purity antimony telluride (Aldrich Prod. No. 740993) to our catalog as a material with applications in thermoelectrics. Antimony telluride alone<sup>1</sup> and in a combination with other metal chalcogenides<sup>2-4</sup> represents a unique class of thermoelectric materials with extremely high thermoelectric figures of merit. In addition, antimony telluride has also drawn substantial attention as a topological insulator, where the anomalous Hall effect is observed as the existence of voltage transverse to an applied current without an external magnetic field.<sup>5-6</sup>

## References

- (1) Poudeu, Pierre F. P.; Kanatzidis, Mercuri G.; *Chemical Communications* (Cambridge, United Kingdom), **2005**, 21, 2672-2674.
- (2) Surinach, S.; Baro, M. D.; Clavaguera-Mora, M. T.; Clavaguera, N.; *Journal of Materials Science*, **1984**, 19(9), 3005-12
- (3) Im, Jae-Taek; Hartwig, K. Ted.; Sharp, Jeff; *Acta Materialia*, **2004**, 52(1), 49-55
- (4) Venkatasubramanian, Rama; Slivola, Edward; Colpitts, Thomas; O'Quinn, Brooks; *Nature*, **2001**, 413(6856), 597-602
- (5) Zhang, Haijun; Liu, Chao-Xing; Qi, Xiao-Liang; Dai, Xi; Fang, Zhong; Zhang, Shou-Cheng; *Nature Physics*, **2009**, 5(6), 438-442.
- (6) Eremeev, S. V.; Koroteev, Yu. M.; Chulkov, E. V.; *JETP Letters*, **2010**, 91(8), 387-391.

## Antimony(III) telluride

Antimony sesquitelluride; Antimony telluride; Sb<sub>2</sub>Te<sub>3</sub>  
Diantimony tritelluride  
[1327-50-0] Sb<sub>2</sub>Te<sub>3</sub> FW 626.32  
density . . . . . 6.5 g/mL, 25 °C

### ► beads, ≥99.99%

Sb<sub>2</sub>Te<sub>3</sub>, along with Bi<sub>2</sub>Te<sub>3</sub> and other structurally analogous semiconductors, is widely regarded as one of the best materials for room temperature thermoelectric devices. Antimony(III) telluride is a key component of thermoelectric materials that have reached ZT values as high as 2.4 at room temperature.

740993-5G 5g

## Electrode Materials for Lithium Ion Batteries



Kinson C. Kam and Marca M. Doeff\*  
Lawrence Berkeley National Laboratory  
Environmental Energy Technologies Division, University of California  
Berkeley, California 94720  
\*mmdoeff@lbl.gov

### Background

In 2010, the rechargeable lithium ion battery market reached ~\$11 billion and continues to grow.<sup>1</sup> Current demand for lithium batteries is dominated by the portable electronics and power tool industries, but emerging automotive applications such as electric vehicles (EVs) and plug-in hybrid electric vehicles (PHEVs) are now claiming a share. It is now possible for consumers to buy lithium ion battery-powered EVs such as the Tesla Model S sedan or Coda, or PHEVs like the Chevrolet Volt or Fisker Karma. For further market penetration, however, experts agree that prices of the batteries will need to come down, and performance and reliability will need to be improved.

The development of Li ion devices began with work on lithium metal batteries and the discovery of intercalation positive electrodes such as  $\text{TiS}_2$  (Aldrich Prod. No. 333492) in the 1970s.<sup>2,3</sup> This was followed soon after by Goodenough's discovery of the layered oxide,  $\text{LiCoO}_2$ ,<sup>4</sup> and discovery of an electrolyte that allowed reversible cycling of a graphite anode.<sup>5</sup> In 1991, Sony commercialized its first rechargeable lithium ion batteries combining a  $\text{LiCoO}_2$  (Aldrich Prod. No. 442704) cathode with a graphite (Aldrich Prod. No. 496588) anode.<sup>6</sup> In this dual intercalation system, also known as a "rocking chair" device, reversible insertion and removal of lithium ions into the electrodes are used as a means to store and deliver charge (Figure 1).

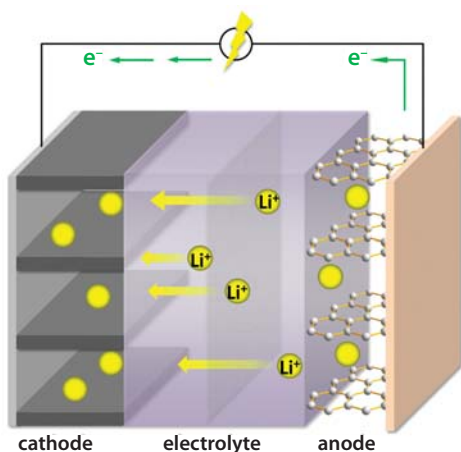


Figure 1. Schematic showing a Li ion battery containing an intercalation cathode on an Al current collector, an electrolytic solution containing a lithium salt, and a graphite anode on a Cu current collector.

Electric current is generated when lithium ions migrate from the negative electrode (anode) to the positive electrode (cathode) through the electrolyte during discharge. Reversing this process results in intercalation of lithium ions back into the anode and their removal from the cathode to produce the charged state. (In practice, cells are first assembled in the discharged state and charged prior to use). Careful cell engineering and improved packaging has resulted in a doubling of energy density over the past 20 years. However, the desire for lower cost and improved performance both for consumer electronic devices and those intended for automotive applications have led researchers to search for and develop alternative cathodes and anodes in the intervening years. Automotive applications, in particular, have stringent requirements for safety, cost, lifetime, and other performance metrics. Goals vary somewhat with the particular application (EV, PHEV, etc.) and a quantitative list can be viewed at: [http://www.uscar.org/guest/article\\_view.php?articles\\_id=85](http://www.uscar.org/guest/article_view.php?articles_id=85) for the interested reader. Although increased energy density is an extremely desirable criterion, safety, calendar and cycle life considerations have sometimes trumped this requirement. Several new electrode materials have been invented over the past 20 years, but there is, as yet, no ideal system that allows battery manufacturers to achieve all of the requirements for vehicular applications. The state of the technology at present is such that there are several competing configurations utilizing different electrode materials, intended for different applications.

### Commercial Battery Electrode Materials

Table 1 lists the characteristics of common commercial positive and negative electrode materials and Figure 2 shows the voltage profiles of selected electrodes in half-cells with lithium anodes. Modern cathodes are either oxides or phosphates containing first row transition metals. There are fewer choices for anodes, which are based on either graphite or the intercalation compound  $\text{Li}_4\text{Ti}_5\text{O}_{12}$  (Aldrich Prod. No. 702277). These materials are lightweight, resulting in high specific capacities and energy densities, and generally perform well, although all have some drawbacks.

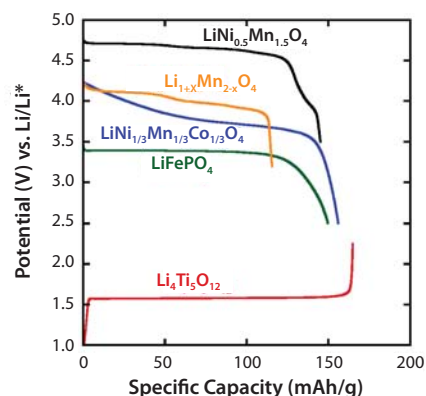


Figure 2. Voltage profiles of selected electrode materials in lithium half-cells.



Table 1. Characteristics of Commercial Battery Electrode Materials

Electrode (Aldrich Prod. No.)	Potential vs. Li/Li <sup>+</sup> (V) <sup>A</sup>	Specific Capacity, (mAh/g)	Advantages	Disadvantages
<b>Positive Electrodes</b>				
LiCoO <sub>2</sub> (442704)	3.9	140	Performance	Cost and resource limitations of Co, low capacity
LiNi <sub>0.8</sub> Co <sub>0.15</sub> Al <sub>0.05</sub> O <sub>2</sub> (760994)	3.8	180–200	High capacity and voltage, excellent rate performance	Safety, cost and resource limitations of Ni and Co
LiNi <sub>1/3</sub> Mn <sub>1/3</sub> Co <sub>1/3</sub> O <sub>2</sub> (761001)	3.8	160–170	High voltage, moderate safety	Cost and resource limitations of Ni and Co
LiMn <sub>2</sub> O <sub>4</sub> variants (725129)	4.1	100–120	Low cost and abundance of Mn, high voltage, moderate safety, excellent rate performance	Limited cycle life, low capacity
LiFePO <sub>4</sub> (759546)	3.45	170	Excellent safety, cycling, and rate capability, low cost and abundance of Fe, low toxicity	Low voltage and capacity (substituted variants), low energy density
<b>Negative Electrodes</b>				
Graphite (698830)	0.1	372	Long cycle life, abundant	Relatively low energy density; inefficiencies due to Solid Electrolyte Interface formation
Li <sub>4</sub> Ti <sub>5</sub> O <sub>12</sub> (765155)	1.5	175	"Zero strain" material, good cycling and efficiencies	High voltage, low capacity (low energy density)

A. Average

## Cathodes

The first intercalation oxide cathode to be discovered, LiCoO<sub>2</sub>, is still in use today in batteries for consumer devices. This compound has the α-NaFeO<sub>2</sub> layer structure (space group R3-m), consisting of a cubic close-packed oxygen array with transition metal and lithium ions occupying octahedral sites in alternating layers (Figure 3). The potential profile of LiCoO<sub>2</sub> in lithium half cells is gradually sloping, and about half the lithium can be removed below 4.2 V vs. Li/Li<sup>+</sup>, to give a specific capacity of 140 mAh/g. Higher capacities can be achieved by increasing the charge voltage limit but this has detrimental effects upon cycle life<sup>7</sup> due to structural instability of the highly delithiated Li<sub>x</sub>CoO<sub>2</sub> compound and irreversible electrolyte oxidation. Resource limitations, the high cost of Co, and the need for higher energy density spurred researchers to investigate other layered transition metal oxides. Out of this research, two new electrodes emerged: LiNi<sub>0.8</sub>Co<sub>0.15</sub>Al<sub>0.05</sub>O<sub>2</sub> (or NCA)<sup>8,9,10,11</sup> (Aldrich Prod. No. 760994) and LiNi<sub>1/3</sub>Mn<sub>1/3</sub>Co<sub>1/3</sub>O<sub>2</sub> (or NMC)<sup>12</sup> (Aldrich Prod. No. 761001). They are isostructural to LiCoO<sub>2</sub> but have higher specific capacities. The structural, chemical, and thermal stabilities are also improved compared to LiCoO<sub>2</sub>.<sup>13</sup> The small amounts of Co in these compounds reduce cost and improve the structure of the materials, compared to the parent compounds (LiNiO<sub>2</sub> for NCA and LiNi<sub>0.5</sub>Mn<sub>0.5</sub>O<sub>2</sub> for NMC). The incorporation of Al in NCA improves the thermal stability, although there are still safety concerns. Low-level partial substitution of Al for Co in NMC also has been shown to improve thermal behavior<sup>14</sup> and cycling stability,<sup>15</sup> while the addition of small amounts of Ti appears to increase practical capacities and improves cycling over an extended voltage range.<sup>16,17</sup>

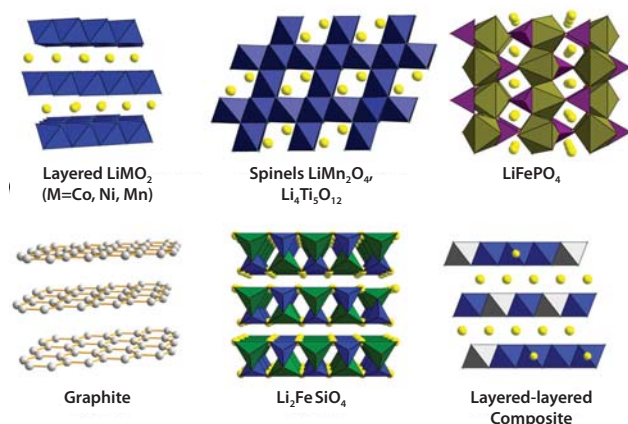
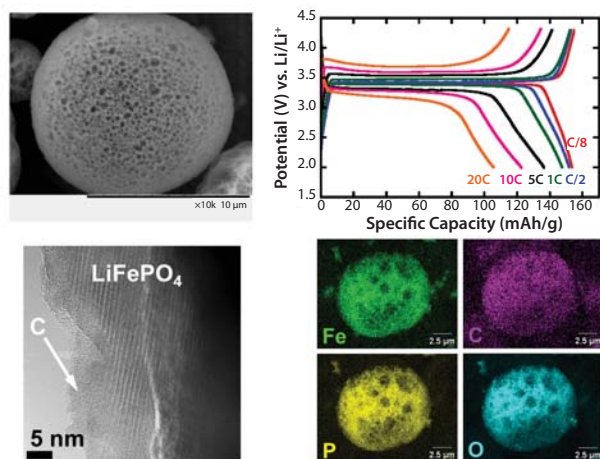


Figure 3. Structures of common electrode materials. From left to right, top: layered LiMO<sub>2</sub> (M=Co, Ni, Mn), spinel structures of LiMn<sub>2</sub>O<sub>4</sub> and Li<sub>4</sub>Ti<sub>5</sub>O<sub>12</sub>, and olivine LiFePO<sub>4</sub>. From left to right, bottom: graphite, Li<sub>2</sub>FeSiO<sub>4</sub>, and the layered-layered composite xLi<sub>2</sub>MnO<sub>3</sub>·(1-x)LiNi<sub>1/3</sub>Mn<sub>1/3</sub>Co<sub>1/3</sub>O<sub>2</sub>. Yellow spheres represent Li ions in these structures and MO<sub>x</sub> units are shown as colored polyhedra. C atoms in graphite are represented as white spheres.

In the Li-Mn-O system, spinels related to the stoichiometric compound LiMn<sub>2</sub>O<sub>4</sub>,<sup>18,19</sup> (Aldrich Prod. No. 482277) are the most technologically important, because LiMnO<sub>2</sub> with the R3-m structure cannot be synthesized directly. While ion exchange of layered NaMnO<sub>2</sub> can be used to produce LiMnO<sub>2</sub> indirectly, it converts to spinel rapidly when cycled in lithium cells.<sup>20</sup> LiMn<sub>2</sub>O<sub>4</sub> has a cubic structure (space group Fd-3m) with Mn located in octahedral 16d sites and Li ions on 8a tetrahedral sites in a cubic close-packed array of oxygen anions (Figure 3). Insertion of Li ions into vacant octahedral sites occurs below 3 V vs. Li/Li<sup>+</sup> and produces the Jahn-Teller distorted tetragonal phase, Li<sub>2</sub>Mn<sub>2</sub>O<sub>4</sub>. There is a 16% elongation of the c-axis upon phase conversion, which causes fracturing and disconnection of particles, and results in rapid capacity fading upon cycling. Removal of Li from the 8a sites to form the delithiated phase, λ-MnO<sub>2</sub>, is much more reversible and occurs above 4 V vs. Li/Li<sup>+</sup>. Thus, cycling is restricted to the 4 V region, resulting in a theoretical specific capacity of 148 mAh/g for the stoichiometric compound. In practice, lithium-rich (Li<sub>1+x</sub>Mn<sub>2-x</sub>O<sub>4</sub>) or Al-substituted modifications,<sup>21,22</sup> which have better performance characteristics than LiMn<sub>2</sub>O<sub>4</sub>, are used commercially. The partial substitution of Li or Al for Mn results in lower theoretical capacities, but greatly decreases the risk of inadvertent over-reduction of Mn below an average oxidation state of 3.5 during cycling, which is associated with production of the Jahn-Teller distorted tetragonal phase. While the performance of manganese oxide spinel electrodes has been greatly improved since they were first reported, they do not cycle as well as other oxides and LiFePO<sub>4</sub>, especially when subjected to elevated temperatures, because of the tendency for Mn to dissolve into the somewhat acidic electrolyte. Capacity fading is modest when spinel electrodes are cycled in lithium half-cells, but more evident in full cells with graphite anodes. This is attributable to the precipitation of dissolved manganese on the graphite anode and disruption of the solid electrolyte interface (SEI). Strategies to ameliorate dissolution include coating particle surfaces<sup>23</sup> and the use of non-fluorinated electrolyte salts,<sup>24,25</sup> and have met with some success. In spite of the cycling performance issues, the low cost and great abundance of Mn and the high power capability of spinel electrodes make them attractive choices for vehicular and some consumer device applications.

In 1997, the phospho-olivine LiFePO<sub>4</sub> was first reported as a cathode material.<sup>26</sup> Its orthorhombic structure contains FeO<sub>6</sub> octahedra and PO<sub>4</sub> tetrahedra networked together to form 1D channels allowing lithium to diffuse along the b-axis (Figure 3). The theoretical specific capacity is ~170 mAh/g and the discharge profile is flat at ~3.45 V (Figure 2), characteristic of a two-phase reaction (LiFePO<sub>4</sub> ↔ FePO<sub>4</sub> + e<sup>-</sup> + Li<sup>+</sup>). The poor utilization and rate capability<sup>27,28</sup> initially reported for this material in electrochemical cells was attributed to its low electronic conductivity and poor transport properties. Nanostructuring and carbon-coating of particles have greatly improved performance, and LiFePO<sub>4</sub> is now considered one of the highest performance electrode materials available.<sup>29</sup> Because the addition of electrochemically inert carbon reduces practical energy density, care must be taken to minimize the

amount of coating on particles.<sup>30,31</sup> Likewise, nanoparticulate powders frequently do not pack well, requiring additional binder and conductive additives in the electrodes, which reduces practical energy density further. Hierarchical structuring, in which small primary particles are organized into larger secondary ones, improves the energy density penalty somewhat. **Figure 4** shows an example of a hierarchically structured composite of  $\text{LiFePO}_4/\text{C}$  with excellent electrochemical performance.<sup>32</sup>



**Figure 4.** Upper left: scanning electron micrograph showing porous  $\text{LiFePO}_4/\text{C}$  particle. Lower left: transmission electron micrograph of an internal surface of a  $\text{LiFePO}_4/\text{C}$  particle showing a thin amorphous carbon coating. Upper right: rate capability of Li cells containing the  $\text{LiFePO}_4/\text{C}$  composites. Lower right: elemental mapping of  $\text{LiFePO}_4/\text{C}$  particle, showing homogeneous distribution. Modified figure from reference 31 used with permission.

In spite of its relatively low energy density, the safety characteristics of the  $\text{LiFePO}_4$  electrode make it attractive for some vehicular applications. The charged material,  $\text{FePO}_4$ , does not evolve oxygen upon heating, but rather converts to an electrochemically inert quartz structure with the same composition.<sup>33</sup> The low voltage at which it operates also means that reactivity with the electrolyte and the associated safety issues are not as much of a concern as they are with the higher voltage oxide electrodes discussed previously. The low reactivity is what has allowed the success of a nanostructuring approach for  $\text{LiFePO}_4$  electrodes. In contrast, nanostructuring of the higher voltage oxide electrodes often leads to accelerated capacity fading upon cycling as well as safety concerns due to increased reactivity of electrolyte with the high surface area particles and accelerated oxygen release. **Figure 5** shows an example of this phenomenon; a nanostructured NMC exhibits higher capacity fade than a conventionally prepared material when cycled to 4.7 V in lithium half-cells.

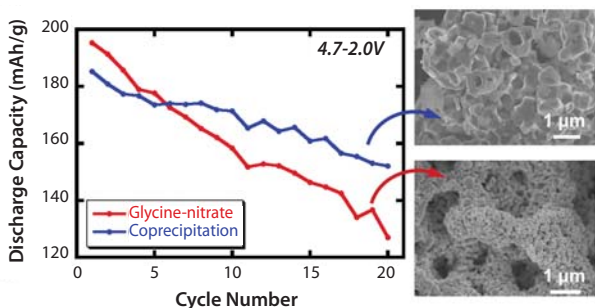


**Figure 5.** Capacity as a function of cycle number for cells cycled at  $0.1 \text{ mA}/\text{cm}^2$  between 4.7–2.0 V, containing two different  $\text{LiNi}_{1/3}\text{Mn}_{1/3}\text{Co}_{1/3}\text{O}_2$  samples, one made by glycine-nitrate combustion, which produces nanoparticles, and the other by a coprecipitation method, which results in micron-sized particles.

## Anodes

At present, there are only two types of commercialized anode materials: those based on carbon (primarily graphite) and the oxide spinel  $\text{Li}_4\text{Ti}_5\text{O}_{12}$  (see **Figure 3** for structures). The use of a low potential intercalation electrode avoids the cycling and safety issues associated with dendrite formation on lithium anodes undergoing recharge, which have stymied their use in rechargeable batteries. Under normal operating and most abuse conditions, lithium dendrites do not grow on graphite anodes, and these electrodes can be cycled reliably. The chemical preparation of the graphite intercalation compounds (GICs)  $\text{Li}_x\text{C}_6$  ( $x=1$ ), in which lithium ions are located between graphene sheets, was first reported in 1955 by Hérold.<sup>34</sup> While lithiated graphite was proposed for use in batteries as early as 1977 by Armand and Touzain,<sup>35</sup> solvent co-intercalation and irreversible reduction of the electrolytic solutions commonly used at the time prevented electrochemical cycling of this electrode. It was not until electrolytic solutions containing ethylene carbonate (EC) (**Aldrich Prod. No. 676802**) were developed that graphite anodes could be used successfully in a lithium ion battery configuration. In these solutions, a solid electrolyte interface (SEI) forms on particle surfaces as graphite is lithiated in electrochemical cells during early cycles. The SEI is ionically conductive but electronically insulating, and, once formed, effectively prevents further irreversible reduction of the electrolytic solution. Some of the electrolyte is necessarily consumed during initial cell cycling to form the SEI, resulting in charge inefficiency. Careful purification, optimization of particle morphologies, and the use of electrolyte additives have reduced the inefficiency considerably; as a result, advanced Li ion batteries exhibit initial irreversible capacities of only a few percent. Precipitation of dissolved metal originating from the cathode or high temperature excursions during operation may disrupt the SEI, thereby necessitating its re-formation; this then results in further loss of cycleable lithium.

Graphite consists of graphene sheets staggered in either an AB (hexagonal, the most common form) or ABC (rhombohedral) stacking arrangement (**Figure 3**). Upon insertion of lithium ions, the graphene sheets stack directly on top of one another in an AA arrangement, and staging occurs; i.e. compounds form in which there are periodic arrays of unoccupied galleries, with the number dependent on the value of  $x$  in  $\text{Li}_x\text{C}_6$ . (For example, in the stage 2 compound where  $x=0.5$ , occupied galleries alternate with unoccupied ones). Staging is manifested in the electrochemical voltage profile of lithium/graphite half-cells as a series of plateaus from about 0.2–0.1 V, indicative of several two-phase regions.

Non-graphitic carbons, which contain graphene domains but do not have long-range structural order, are also of interest for lithium ion batteries. Lithium insertion into these materials usually occurs at higher potentials than graphite, and staging does not occur. While the irreversible capacities are often much higher than with graphite, the SEI on some types of disordered carbon (e.g., hard carbons) are less susceptible to disruption, making them suitable for pairing with manganese oxide spinel cathodes in which metal dissolution can be problematic. The structures of disordered carbons are highly complex, and the electrochemical properties (shape of the voltage profile and capacity) vary considerably. For further information on carbon anodes, the reader is directed to references 36 and 37.



The spinel lithium titanium oxide,  $\text{Li}_4\text{Ti}_5\text{O}_{12}$ ,<sup>38</sup> (Aldrich Prod. No. 702277) is an alternative to carbon anodes, but its use is restricted to applications that do not require high energy density because of its high operating voltage (1.5 V vs.  $\text{Li}/\text{Li}^+$ ). It reversibly accommodates lithium to form the rock salt phase,  $\text{Li}_7\text{Ti}_4\text{O}_{12}$ . Unlike most other intercalation electrodes, this material exhibits no volume change during the two-phase lithium insertion/extraction processes, making it a zero-strain material that cycles extremely well.<sup>39</sup> Additionally, a high operating potential occurs within the thermodynamic stability window of organic carbonate-based electrolytic solutions, so that it is not necessary to form an SEI layer for proper functioning of the electrode. Because  $\text{Li}_4\text{Ti}_5\text{O}_{12}$  has intrinsically low electronic conductivity, it is often nanostructured. As with  $\text{LiFePO}_4$ , the low reactivity of  $\text{Li}_4\text{Ti}_5\text{O}_{12}$  is what allows this approach to succeed, although concerns about the effect of nanostructuring on the already low energy density are still warranted. Best results are obtained when nanoparticles are uniform and spherical so that they pack well.<sup>40</sup> Cells consisting of nanostructured  $\text{Li}_4\text{Ti}_5\text{O}_{12}$  and  $\text{LiFePO}_4$  could be cycled over 200 times at rates up to 10 C (where C is defined as the rate at which the total capacity of the cell is discharged in 1 hour) with no capacity fading.

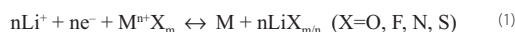
## Toward Better Batteries

Current research on electrodes for Li ion batteries is directed primarily toward materials that can enable higher energy density of devices. For positive electrodes, both high voltage materials such as  $\text{LiNi}_{0.5}\text{Mn}_{1.5}\text{O}_4$  (Aldrich Prod. No. 725110) (Figure 2) and those with increased capacity are under development. The latter include the high capacity manganese-rich (HCMR) layered-layered composites with the general formula  $x\text{Li}_2\text{MnO}_3 \cdot (1-x)\text{LiNi}_y\text{Mn}_y\text{Co}_{1-2y}\text{O}_2$ ,<sup>41</sup> and compounds such as  $\text{Li}_2\text{MSiO}_4$  ( $M=\text{Fe}, \text{Mn}, \text{Co}$ ) in which more than one Li per formula unit can, in theory, be removed. For the layered-layered composites, an initial charge above about 4.4 V vs.  $\text{Li}/\text{Li}^+$  in electrochemical cells activates the normally inert  $\text{Li}_2\text{MnO}_3$  component by removing lithium ions and oxygen irreversibly. The layered “ $\text{MnO}_2$ ” moiety that is formed can then intercalate lithium ions, adding its capacity to that of the NMC component. While very high capacities (sometimes in excess of 250 mAh/g) have been reported for the activated composites in electrochemical cells, they suffer from poor rate capability and voltage decay due to the gradual conversion of the layered  $\text{MnO}_2$  component to spinel upon cycling.

The high theoretical capacity of about 330 mAh/g calculated for  $\text{Li}_2\text{MSiO}_4$  based on extraction of two lithium ions per formula unit requires an overall redox state change of +2 for the initially divalent metal center. First principles calculations indicate that oxidation of  $\text{Fe}^{3+}$  to  $\text{Fe}^{4+}$  occurs at an impractically high potential,<sup>42</sup> and experiments have verified that only the first lithium ion can be extracted during charge of  $\text{Li}_2\text{FeSiO}_4$  in electrochemical cells.<sup>43</sup> While the oxidation of  $\text{Mn}^{3+}$  to  $\text{Mn}^{4+}$  in the silicates is expected to occur at lower potentials than that of  $\text{Fe}^{3+}$  to  $\text{Fe}^{4+}$ , attempts to use  $\text{Li}_2\text{MnSiO}_4$  or  $\text{Li}_2(\text{Mn},\text{Fe})\text{SiO}_4$  compounds as cathodes have not met with much success. Even nanostructuring and the addition of large amounts of carbon to composite electrodes do not sufficiently compensate for the poor transport properties and have a negative impact on practical energy density. In addition, the wide voltage range over which the intercalation processes occur is undesirable since it leads to a decay of power capability as the electrode discharges. Compounds in which metal centers can undergo more than one change in oxidation state remain of interest because of the potential for very high capacities, and researchers are continuing to search for electroactive materials with these characteristics.

In contrast, the high voltage spinel cathode  $\text{LiNi}_{0.5}\text{Mn}_{1.5}\text{O}_4$  exhibits very good rate and cycling performance without requiring nanostructuring,<sup>44</sup> although the energy density advantage over commercially used materials is relatively modest (only about 30% greater than for  $\text{Li}_{1+x}\text{Mn}_{2-x}\text{O}_4$ , for example). The high operating potential may require the use of specially designed electrolytic solutions, coatings on particle surfaces, and other strategies to reduce coulombic inefficiencies and prolong cycle life. As with the isostructural  $\text{LiMn}_2\text{O}_4$  variants, dissolution of Mn is potentially a problem for cycle life. This phenomenon, in both cases, is associated with the presence of electroactive  $\text{Mn}^{3+}$ . In the idealized structure of  $\text{LiNi}_{0.5}\text{Mn}_{1.5}\text{O}_4$ , Mn ions are in the +4 oxidation state and are electrochemically inert, and only Ni undergoes redox processes. In practice, samples usually exhibit some degree of non-stoichiometry, with excess Mn present in the trivalent state. This is manifested in the potential profile as capacity at about 4 V vs.  $\text{Li}/\text{Li}^+$  (Figure 2).

Research into new anode materials has been focused on Li alloys, primarily with Si,<sup>45</sup> (Aldrich Prod. No. 633097) and a class of materials known as conversion electrodes,<sup>46</sup> which undergo Reaction 1 rather than simple intercalation.



The starting materials for Reaction 1 are generally nanoparticulate, allowing facile reduction to the metallic element and lithium salt during lithium incorporation. Specific capacities can be extremely high (700 mAh/g or more), but these electrodes are plagued by high first-cycle inefficiencies, sloping voltage profiles, and large charge/discharge polarizations (hysteresis) leading to poor round-trip efficiencies. The hysteresis is most likely intrinsic to the system rather than a simple matter of kinetic limitations, which presumably could be ameliorated by nanostructuring. Bond breaking and re-formation occurs during the electrochemical processes, and reaction pathways may not be the same for charge and discharge.

The silicon/lithium system has the highest specific capacity of any lithium alloy, 4,200 mAh/g, corresponding to reduction all the way to the end-member composition of  $\text{Li}_{4.4}\text{Si}$ . The very large volume changes associated with alloying (up to 400%) lead to rapid degradation and disconnection in composite electrodes prepared from conventional micron-sized silicon so that cycle life is poor.<sup>47</sup> The volume changes also result in large coulombic inefficiencies associated with the continual formation of SEI layers on freshly exposed surfaces. Considerable efforts have been made to lower the volume expansion by nanostructuring Si to reduce mechanical stresses during the lithium alloying/de-alloying processes.<sup>48</sup> Other strategies that have met with some success include the use of special binders that provide elasticity to the composite electrode,<sup>49</sup> as well as conductive polymers which serve a dual purpose as binder and conductive additive.<sup>50</sup>

Small amounts of silicon are currently added to commercial anodes to boost capacity, and several battery companies have announced their intentions to replace graphite with silicon. Somewhat surprisingly, the improvement in specific energy of batteries containing Si anodes is expected to be only about 30%, in spite of the fact that the specific capacity of silicon is more than ten times greater than that of graphite. This is because of the requirement for capacity matching of the anode and the much less energy dense cathode, which must provide all of the cycleable lithium in the battery. Further increases in specific energy are, therefore, contingent upon successful development of a higher capacity cathode.

## Summary and Challenges

The need for improved lithium ion batteries for demanding vehicular applications provides both challenges and opportunities for the interested materials scientist. While higher energy density is extremely desirable for these applications as well as for consumer electronics, it cannot come at the cost of safety, cycle life, or calendar life (Figure 5). For this reason, nanostructuring works best when used on materials with low reactivity, such as  $\text{LiFePO}_4$  and  $\text{Li}_4\text{Ti}_5\text{O}_{12}$ , which have now been commercialized. A nano approach also appears to have some merit for silicon anodes, which are in an advanced stage of development. In addition to silicon, new high-energy density electrodes such as layered-layered oxide composites, high voltage spinels, conversion materials, and multivalent redox compounds including but not limited to silicates have recently emerged on the battery landscape.

## Acknowledgment

This work was supported by the Assistant Secretary for Energy Efficiency and Renewable Energy, Office of Vehicle Technologies of the U.S. Department of Energy under Contract No. DE-AC02-05CH11231. This document was prepared as an account of work sponsored by the United States Government. While this document is believed to contain correct information, neither the United States Government nor any agency thereof, nor the Regents of the University of California, nor any of their employees, makes any warranty, express or implied, or assumes any legal responsibility for the accuracy, completeness, or usefulness of any information, apparatus, product, or process disclosed, or represents that its use would not infringe privately owned rights. Reference herein to any specific commercial product, process, or service by its trade name, trademark, manufacturer, or otherwise, does not necessarily constitute or imply its endorsement, recommendation, or favoring by the United States Government or any agency thereof, or the Regents of the University of California. The views and opinions of authors expressed herein do not necessarily state or reflect those of the United States Government or any agency thereof or the Regents of the University of California.

## References

- "Lithium Ion Batteries Outlook And Alternative Energy Vehicles (Hevs, Phevs, Evs)-Technologies, Markets, Competitors And Opportunities: 2010-2020 Analysis And Forecasts" MarketResearch.com, Rockville, MD. <http://www.marketresearch.com/David-Company-v3832/Lithium-Ion-Batteries-Outlook-Alternative-6842261/>
- Whittingham, M. S.; Gamble, F.R., *Mater. Res. Bull.*, **1975**, *10*, 363.
- Whittingham, M. S., *J. Electrochem. Soc.*, **1976**, *123*, 315.
- Mizushima, K.; Jones, P. C.; Wiseman, P. J.; Goodenough, J. B., *Mater. Res. Bull.*, **1980**, *15*, 783.
- Fong, R.; von Sacken, U.; Dahn, J. R., *J. Electrochem. Soc.*, **1990**, *137*, 2009.
- Nagaura, T.; Tozawa, K., *Progress in Batteries and Solar Cells*; JECs Press Inc., Brunswick, OH, **1990**, vol. 9, 209.
- Chen, Z.; Lu, Z.; Dahn, J. R., *J. Electrochem. Soc.*, **2002**, *149*, A1604.
- Dahn, J. R.; Zhao, X.; Lu, Z.; Jiang, J.; Dahn, J. R., *Electrochem. Commun.*, **1994**, *69*, 265.
- Albrecht, S.; Kümpers, J.; Kruff, M.; Malcus, S.; Vogler, C.; Wahl, M.; Wohlfahrt-Mehrens, M., *J. Power Sources*, **2003**, *119-121*, 178.
- Chen, C. H.; Liu, J.; Stoll, M. E.; Henriksen, G.; Vissers, D. R.; Amine, K., *J. Power Sources*, **2004**, *128*, 278.
- Kostecki, R.; Lei, J.; McLarnon, F.; Shim, J.; Striebel, K., *J. Electrochem. Soc.*, **2006**, *153*, A669.
- Yabuuchi, N.; Ohzuku, T., *J. Power Sources*, **2003**, *119-121*, 171.
- Choi, J.; Manthiram, A., *J. Electrochem. Soc.*, **2005**, *152*, A1714.
- Zhou, F.; Zhao, X.; Lu, Z.; Jiang, J.; Dahn, J. R., *Electrochem. Commun.*, **2008**, *10*, 1054.
- Wilcox, J. D.; Rodriguez, E. E.; Doeff, M. M., *J. Electrochem. Soc.*, **2009**, *156*, A1011.
- Kam, K. C.; Doeff, M. M., *J. Mater. Chem.*, **2011**, *21*, 9991.
- Kam, K. C.; Mehta, A.; Heron, J. T.; Doeff, M. M., *J. Electrochem. Soc.*, **2012**, *159*, A1383.
- Thackeray, M. M.; David, W. I. F.; Bruce, P. G.; Goodenough, J. B., *Mater. Res. Bull.*, **1983**, *18*, 461.
- Tarascon, J. M.; McKinnon, W. R.; Coowar, F.; Bowmer, T. N.; Amatucci, G.; Guyomard, D., *J. Electrochem. Soc.*, **1994**, *141*, 1421.
- Armstrong, A. R.; Bruce, P. G., *Nature*, **1996**, *381*, 499.
- Gummow, R. J.; de Kock, A.; Thackeray, M. M., *Solid State Ionics*, **1994**, *69*, 59.
- Ariyoshi, K.; Iwata, E.; Kuniyoshi, M.; Wakabayashi, H.; Ohzuku, T., *Electrochem. Solid St.*, **2006**, *9*, A557.
- Cho, J.; Kim, G. B.; Lim, H. S.; Kim, C.-S.; Yoo, S.-I., *Electrochem. Solid St.*, **1999**, *2*, 607.
- Xu, K.; Zhang, S.; Jow, T. R.; Xu, W.; Angell, C. A., *Electrochem. Solid St.*, **2002**, *5*, A26.
- Chen, Z.; Amine, K., *J. Electrochem. Soc.*, **2006**, *153*, A316.
- Padhi, A. K.; Nanjundaswamy, K. S.; Goodenough, J. B., *J. Electrochem. Soc.*, **1997**, *144*, 1188.
- Andersson, A. S.; Thomas, J. O.; Kalska, B.; Häggström, L., *Electrochem. Solid St.*, **2000**, *3*, 66.
- Yamada, A.; Chung, S. C.; Hinokuma, K., *J. Electrochem. Soc.*, **2001**, *148*, A224.
- Kang, B.; Ceder, G., *Nature*, **2009**, *458*, 190.
- Doeff, M. M.; Hu, Y. Q.; McLarnon, F.; Kostecki, R., *Electrochem. Solid St.*, **2003**, *6*, A207.
- Wilcox, J. D.; Doeff, M. M.; Marcinek, M.; Kostecki, R., *J. Electrochem. Soc.*, **2007**, *154*, A389.
- Liu, J.; Conry, T. E.; Song, X. Y.; Doeff, M. M.; Richardson, T. J., *Energ. Environ. Sci.*, **2011**, *4*, 885.
- Yang, S.; Song, Y.; Zavalij, P. Y.; Whittingham, M. S., *Electrochem. Commun.*, **2002**, *4*, 239.
- Hérol, A., *B. Soc. Chim. Fr.*, **1955**, *7-8*, 999.
- Armand, M.; Touzain, P., *Mater. Sci. Eng.*, **1977**, *31*, 319.
- Winter, M.; Besenhard, J. O.; Spahr, M. E.; Novak, P., *Adv. Mater.*, **1998**, *10*, 725.
- Flandrois, S.; Simon, B., *Carbon*, **1999**, *37*, 165.
- Ferg, E.; Gummow, R. J.; de Kock, A.; Thackeray, M. M., *J. Electrochem. Soc.*, **1994**, *141*, L147.
- Ohzuku, T.; Ueda, A.; Yamamoto, N., *J. Electrochem. Soc.*, **1995**, *142*, 1431.
- Jaiswal, A.; Horne, C. R.; Chang, O.; Zhang, W.; Kong, W.; Wang, E.; Chern, T.; Doeff, M. M., *J. Electrochem. Soc.*, **2009**, *156*, A1041.
- Thackeray, M. M.; Kang, S. H.; Johnson, C. S.; Vaughey, J. T.; Benedek, R.; Hackney, S. A., *J. Mater. Chem.*, **2007**, *17*, 3112.
- Arroyo-de Dompablo, M. E.; Armand, M.; Tarascon, J. M.; Amador, U., *Electrochem. Commun.*, **2006**, *8*, 1292.
- Kam, K. C.; Gustafsson, T.; Thomas, J. O., **2011**, *192*, 356.
- Cabana, J.; Zheng, H.; Shukla, A. K.; Kim, C.; Battaglia, V. S.; Kunduraci, M., *J. Electrochem. Soc.*, **2011**, *158*, A997.
- Winter, M.; Besenhard, J. O., *Electrochim. Acta*, **1999**, *45*, 31.
- Cabana, J.; Monconduit, L.; Larcher, D.; Palacin, M. R., *Adv. Mater.*, **2010**, *22*, E170.
- Kasavajula, U.; Wang, C. S.; Appleby, A. J., *J. Power Sources*, **2007**, *163*, 1003.
- Chan, C. K.; Peng, H.; Liu, G.; McIlwrath, K.; Zhang, X. F.; Huggins, R. A.; Cui, Y., *Nature Nanotech.*, **2008**, *3*, 31.
- Hochgatterer, N. S.; Schweiger, M. R.; Koller, S.; Raimann, P. R.; Wöhrle, T.; Wurm, C.; Winter, M., *Electrochem. Solid St.*, **2008**, *11*, A76.
- Liu, G.; Xun, S. D.; Vukmirovic, N.; Song, X. Y.; Olalde-Velasco, P.; Zheng, H. H.; Battaglia, V. S.; Wang, L. W.; Yang, W. L., *Adv. Mater.*, **2011**, *23*, 4679.



## Electrode Sheets

Sheet Size: 5" x 10" / 80% active material on aluminum electrode substrate.

For a complete list of available materials, visit [aldrich.com/lib](http://aldrich.com/lib).

Name	Composition	Purity	Nominal Voltage (V)	Capacity (minimum)	Capacity (nominal)	Prod. No.
Lithium titanate, LTO	$\text{Li}_4\text{Ti}_5\text{O}_{12}$	>98%	1.5 (Li/Li <sup>+</sup> )	150 mAh/g	160 mAh/g	765155-1EA
Lithium nickel manganese cobalt oxide, NMC	$\text{LiNi}_{0.33}\text{Mn}_{0.33}\text{Co}_{0.33}\text{O}_2$	>99%	3.5 (Li/Li <sup>+</sup> )	210 mAh/g	250 mAh/g	765163-1EA
Lithium nickel cobalt aluminium oxide, NCA	$\text{LiNi}_{0.8}\text{Co}_{0.15}\text{Al}_{0.05}\text{O}_2$	>98%	3.7 (Li/Li <sup>+</sup> )	150 mAh/g	180 mAh/g	765171-1EA
Lithium manganese nickel oxide, LMNO	$\text{Li}_2\text{Mn}_3\text{NiO}_8$	>98%	4.7 (Li/Li <sup>+</sup> )	125 mAh/g	115 mAh/g	765198-1EA
Lithium manganese(III,IV) oxide, LMO	$\text{LiMn}_2\text{O}_4$	>98%	4.7 (Li/Li <sup>+</sup> )	120 mAh/g	110 mAh/g	765201-1EA

## Cathode Materials

For a complete list of available materials, visit [aldrich.com/lib](http://aldrich.com/lib).

Name	Composition	Purity	Description	Prod. No.
Lithium nickel manganese cobalt oxide, NMC	$\text{LiNi}_{0.33}\text{Mn}_{0.33}\text{Co}_{0.33}\text{O}_2$	>98%	particle size <0.5 μm, powder	761001-10G
Lithium nickel cobalt aluminium oxide, NCA	$\text{LiNi}_{0.8}\text{Co}_{0.15}\text{Al}_{0.05}\text{O}_2$	>98%	particle size <0.5 μm, powder	760994-10G
Lithium nickel cobalt oxide, LNCO	$\text{LiNi}_{0.8}\text{Co}_{0.2}\text{O}_2$	>98%	particle size <0.5 μm	760986-10G
Lithium iron phosphate, LFP	$\text{LiFePO}_4$	>98%	particle size <0.5 μm, powder	759546-5G
Lithium nickel dioxide, LNO	$\text{LiNiO}_2$	>98%	particle size <3 μm, powder	757365-10G
Lithium trivanadate, LTV	$\text{LiV}_2\text{O}_8$	98%	powder	771511-5G
Manganese nickel carbonate	$\text{Mn}_{0.75}\text{Ni}_{0.25}\text{CO}_3$	99.99% trace metals basis	powder	763608-25G
Copper(II) vanadium oxide	$\text{CuV}_2\text{O}_6$	99.7% trace metals basis	powder	763683-50G
Cobalt(IV) sulfide	$\text{CoS}_2$	≥99.5% trace metals basis	powder	764566-25G
Germanium(IV) sulfide	$\text{GeS}_2$	>99.999% trace metals basis	particle size -80 mesh, powder	756466-5G
Lithium cobalt phosphate, LCP	$\text{LiCoPO}_4$	99%	powder	725145-25G
Lithium manganese dioxide	$\text{LiMnO}_2$	>99% trace metals basis	particle size <1 μm, powder	725137-25G
Lithium manganese oxide, LMO	$\text{LiMn}_2\text{O}_4$	>99%	particle size <0.5 μm (BET), powder	725129-25G
Lithium manganese nickel oxide, LMNO	$\text{Li}_2\text{Mn}_3\text{NiO}_8$	>99%	particle size <0.5 μm (BET), powder	725110-25G
Lithium manganese(III,IV) oxide, LMO	$\text{LiMn}_2\text{O}_4$	-	particle size <5 μm	482277-25G
Lithium iron(III) oxide	$\text{LiFeO}_2$	95%	particle size <1 μm, powder	442712-100G-A
Lithium cobalt(III) oxide	$\text{LiCoO}_2$	99.8% trace metals basis	powder	442704-100G-A
Lithium molybdate	$\text{Li}_2\text{MoO}_4$	99.9% trace metals basis	powder or crystals	400904-250G

## Anode Materials: Lithium, Titanate and Tin

For a complete list of available materials, visit [aldrich.com/lib](http://aldrich.com/lib).

Name	Composition	Purity	Dimensions	Form	Prod. No.
Lithium titanate, spinel	$\text{Li}_4\text{Ti}_5\text{O}_{12}$	>99%	particle size <100 nm (BET)	nanopowder	702277-25G
Lithium titanate	$\text{Li}_2\text{TiO}_3$	-	-325 mesh	powder	400939-100G
Lithium-aluminum alloy	Al-Li	-	-	powder	426490-25G
Lithium	Li	99.9% trace metals basis	thickness x W 0.38 x 23 mm	ribbon	265985-25G 265985-100G
Lithium	Li	99.9% trace metals basis	thickness x W 0.75 x 45 mm	ribbon	265993-25G 265993-100G
Lithium	Li	99.9% trace metals basis	thickness x W 1.5 x 100 mm	ribbon	266000-25G 266000-100G
Lithium	Li	≥98%	diam. 3.2 mm	wire	278327-25G 278327-100G
Lithium	Li	99.9% trace metals basis	thickness x W 0.75 x 19 mm	ribbon	320080-25G 320080-100G
Lithium	Li	99%, metals basis	particle size 4-10 mesh	granular	444456-10G 444456-50G
Tin(IV) oxide	$\text{SnO}_2$	-	particle size <100 nm (BET)	nanopowder	549657-5G 549657-25G

## Anode Materials: Carbon and Silicon

For a complete list of available materials, visit [aldrich.com/periodic](http://aldrich.com/periodic).

Name	Purity	Particle Size	Form	Prod. No.
Graphite	98% carbon basis	100 nm (average width, TEM) 2.5 $\mu\text{m}$ (average length, TEM)	powder	698830-1G
Graphite	95% trace metals basis	particle size 200-500 nm	powder	636398-2G 636398-10G
Graphite	99.99% trace metals basis	<150 $\mu\text{m}$	powder	496588-113.4G
Graphite	$\geq 99.99\%$	<45 $\mu\text{m}$	powder	496596-113.4G
Graphite	-	<20 $\mu\text{m}$	powder	282863-25G 282863-1KG
Carbon, mesoporous	>99.95% trace metals basis	particle size <500 nm (DLS)	nanopowder	699624-5G 699624-25G
Carbon	$\geq 99\%$ trace metals basis	particle size <50 nm (TEM)	nanopowder	633100-25G 633100-100G
Carbon	99.95% trace metals basis	2 - 12 $\mu\text{m}$	glassy, spherical powder	484164-10G 484164-50G
Silicon	$\geq 98\%$ trace metals basis	particle size <100 nm (TEM)	nanopowder	633097-10G 633097-25G
Silicon	99% trace metals basis	-325 mesh	powder	215619-50G 215619-250G 215619-1KG
Silicon	99.999% trace metals basis	-60 mesh	powder	267414-25G
Silicon	99.95% trace metals basis	-	pieces	343250-50G 343250-500G

## Electrolyte Materials

For a complete list of available materials, visit [aldrich.com/lib](http://aldrich.com/lib).

Name	Composition	Purity	Form	Prod. No.
Lithium bis(oxalato)borate	$\text{LiB}(\text{C}_2\text{O}_4)_2$	-	powder or crystals	757136-25G
Lithium tetrachlorogallate	$\text{LiGaCl}_4$	99.99% trace metals basis	beads	736317-5G
Lithium perchlorate	$\text{LiClO}_4$	99.99% trace metals basis	powder and chunks	634565-10G 634565-100G
Lithium hexafluorophosphate	$\text{LiPF}_6$	$\geq 99.99\%$ trace metals basis	powder	450227-5G 450227-25G
Lithium trifluoromethanesulfonate	$\text{CF}_3\text{SO}_3\text{Li}$	99.995% trace metals basis	powder	481548-5G 481548-25G
Lithium tetrachloroaluminate	$\text{LiAlCl}_4$	99.99% trace metals basis	beads	451142-5G
Lithium tetrafluoroborate	$\text{LiBF}_4$	99.998% trace metals basis	powder	451622-5G 451622-25G
Lithium hexafluoroarsenate(V)	$\text{LiAsF}_6$	98%	powder	308315-10G
Lithium phosphate monobasic	$\text{LiH}_2\text{PO}_4$	99%	powder or crystals	442682-500G-A

## Solvents and Additives

For a complete list of available materials, visit [aldrich.com/lib](http://aldrich.com/lib).

Name	Composition	Purity	Prod. No.
Vinylene carbonate, VC	$\text{C}_3\text{H}_2\text{O}_3$	99%	757144-25G
Fluoroethylene carbonate, FEC	$\text{C}_3\text{H}_3\text{FO}_3$	99%	757349-25G
Ethyl methyl carbonate, EMC	$\text{C}_4\text{H}_8\text{O}_3$	99%	754935-50ML
3-(Methylsulfonyl)-1-propyne	$\text{C}_4\text{H}_6\text{O}_2\text{S}$	95%	718319-5G
Allyl methyl sulfone, MAS	$\text{C}_4\text{H}_8\text{O}_2\text{S}$	96%	718203-5G
Diethyl carbonate, DEC	$\text{C}_5\text{H}_{10}\text{O}_3$	$\geq 99\%$	517135-100ML 517135-1L
Dimethyl carbonate, DMC	$\text{C}_3\text{H}_6\text{O}_3$	$\geq 99\%$	517127-100ML 517127-1L 517127-2L 517127-20L
Propylene carbonate, PC	$\text{C}_4\text{H}_6\text{O}_3$	99.7%	310328-100ML 310328-500ML 310328-1L 310328-2L

# Quantum Dots

## Core-Type, Core-Shell and Alloyed Nanocrystals



For a complete list of different types of quantum dots available in

- aqueous and organic formulations
- emitting different colors
- high quantum yield

and detailed product information, including a list of availability in your country, visit

[aldrich.com/quantumdots](http://aldrich.com/quantumdots)

Quantum dots are semiconductor nanocrystals with particle dimensions in the range of 2–10 nm, exhibiting both photo- and electroluminescence properties. They can be fine-tuned to emit any color of light by simply changing the material's crystallite size.

Quantum dots can be used for LEDs and solid-state lighting, displays, photovoltaics, transistors, quantum computing, medical imaging, biosensors, among many others.

Our products can be classified into three major types.

**Core-Type Quantum Dots:** uniform, single-component materials, such as zinc or cadmium chalcogenides. Examples include:

- Lumidot™ CdS,  $\lambda_{em}$  380 nm, in toluene ([Prod. No. 662429](#))
- Lumidot™ CdSe,  $\lambda_{em}$  480 nm, in toluene ([Prod. No. 662356](#))
- Lumidot™ CdS-6, quantum dots kit,  $\lambda_{em}$  380–480 nm ([Prod. No. 662593](#))
- Lumidot™ CdSe-6, quantum dots kit,  $\lambda_{em}$  480–640 nm ([Prod. No. 662550](#))

**Core-Shell Quantum Dots:** two-component materials where the external shell improves quantum yield and stability of the nanocrystal. Examples include:

- CdSe/ZnS,  $\lambda_{em}$  485 nm, in toluene/aliphatic amine ([Prod. No. 731862](#))
- CdSe/ZnS,  $\lambda_{em}$  635 nm, in toluene/aliphatic amine ([Prod. No. 731870](#))

**Alloyed Quantum Dots:** multicomponent materials with gradient composition regions determining the optical and electronic properties of the nanocrystal. Examples include:

- CdS<sub>x</sub>Se<sub>1-x</sub>/ZnS,  $\lambda_{em}$  450 nm, 6 nm diameter, in toluene ([Prod. No. 753742](#))
- CdS<sub>x</sub>Se<sub>1-x</sub>/ZnS, carboxyl functionalized,  $\lambda_{em}$  525 nm, 6 nm diameter, in water ([Prod. No. 753831](#))
- CdS<sub>x</sub>Se<sub>1-x</sub>/ZnS-5 quantum dots kit,  $\lambda_{em}$  490–665 nm, 6 nm diameter, in toluene ([Prod. No. 753823](#))
- CdS<sub>x</sub>Se<sub>1-x</sub>/ZnS-5 quantum dots kit, carboxyl functionalized,  $\lambda_{em}$  490–655 nm, 6 nm diameter, in water ([Prod. No. 753904](#))

## Surface-enhanced Solar Energy Conversion Systems Using Gold and Silver Nanoparticles



Shanlin Pan\* and Arunava Gupta  
Department of Chemistry, The University of Alabama  
Tuscaloosa, Alabama 35487-0336  
\*span1@bama.ua.edu

### Solar Energy Conversion and Challenges

Sustainable, environment-friendly, and clean energy sources with sufficiently high production efficiency for practical application are highly desirable to meet the energy challenge of the 21<sup>st</sup> century due to the world's increasing energy demand. The sun provides  $1.2 \times 10^{15}$  TW of light for the earth and only a small fraction of the total solar energy is needed to solve the global energy problem should it be used efficiently for direct electricity generation through solar cell panels and/or clean fuel (e.g., hydrogen production through water splitting). Enormous progress has been made in recent years toward efficient and economic solar energy conversion systems. As an alternative to crystalline silicon, low-cost, stable, and high-efficiency solar cells have been developed to capture solar energy to produce electricity. Amorphous silicon has been used for solar cell panels with only limited efficiency and its production is based on energy-intensive techniques. Several types of organic photovoltaics (OPVs) have been developed as alternatives.<sup>1,2,3,4</sup> OPVs also have limited efficiency because of the conflicting need between a thick donor layer for maximum light absorption and the bottleneck of short exciton diffusion distance.<sup>5</sup> Poor charge-transport mobility and stability of organic semiconductors are additional factors currently limiting the overall device performance. Therefore, new solar energy conversion devices that can support efficient light absorption and hole carrier/exciton transport are highly desirable. Direct water splitting through photoelectrochemical systems continues to hold the promise of providing a practical method for producing high purity hydrogen which can be further used for energy generation, industrial processes and storage.

The ideal photocatalyst for water splitting must satisfy at least four criteria.<sup>6</sup> First, a band gap of  $\sim 2.0$  eV, which corresponds to the equilibrium potential difference between the hydrogen evolution reaction ( $E^0=0.0$  V) and the oxygen evolution reaction ( $E^0=1.23$  V) at 25 °C, and the energy losses in the semiconductor for charge carrier transport. This energy gap corresponds to a 650 nm wavelength incident light absorption. That means a photocatalyst excited with a wavelength shorter than 650 nm is needed for direct water splitting in a single-photon absorption configuration. Tandem cell and/or multiple light absorption configurations would be necessary should a wavelength longer than 650 nm be used for this photochemical reaction.

Second, the valence band edge energy level of the photocatalyst (n-type semiconductor) should be lower than the  $H_2O/O_2$  level, and the Fermi level should be higher than the  $H_2/H_2O$  level in order to obtain direct water splitting under sunlight. External bias and/or interface potential are required if one of two energy level conditions are not satisfied. Third, the photocatalysts must be stable in aqueous solution to avoid degradation that may be caused by photocorrosion. And lastly, the photocatalyst material used for direct water splitting should be inexpensive to be commercially available worldwide. Fujishima and Honda<sup>7</sup> used  $TiO_2$  (Aldrich Prod. No. 224227) as a photoelectrode for water splitting at low efficiency, yet this semiconducting material cannot split water effectively due to its wide band gap, even though it meets all four requirements. Photocatalysts for direct water splitting that absorb in the visible spectrum have been intensely investigated since then.<sup>8</sup> The search for more suitable semiconductors has continued, including new types of oxynitrides [e.g.,  $(Ga_{1-x}Zn_x)(N_{1-x}O_x)$ ]<sup>9</sup> and doped  $TiO_2$  for water splitting using visible light.<sup>10,11</sup>

Hematite ( $\alpha-Fe_2O_3$ ) (Aldrich Prod. No. 529311) has a favorable band gap of around 2.0 eV, is chemically stable in aqueous environments, and is one of the most abundant materials on Earth. Theoretically, a 16.8% water splitting efficiency is predicted for hematite.<sup>12</sup> Hematite also possesses a conduction band edge at an energy level below the  $H_2/H_2O$  level. Thus, one needs to either apply an external electrical bias or couple the hematite electrode with a solar cell in order to enable the water splitting reaction. For example, unassisted solar hydrogen production can be achieved by incorporating hematite in a tandem cell configuration.<sup>13,14</sup> Moreover, while hematite has a light penetration depth of 118 nm (at  $\lambda=550$  nm),<sup>15</sup> it has a very small hole diffusion length (2–4 nm).<sup>16,17</sup> This means the majority of the photons absorbed by a relatively thick hematite layer cannot be used to oxidize water at the solid-liquid interface. This problem can be partially addressed by using nanoscale materials and doping agents. For example, silicon-doped hematite thin films and nanostructures, prepared by atmospheric pressure chemical vapor deposition (APCVD),<sup>18</sup> can have a variety of nanostructured morphologies and exhibit a solar-to-hydrogen conversion efficiency of 3% in a tandem configuration. Thus, a different methodology is needed to further improve the overall photoelectrochemical performance of a visible-light-active photocatalyst such as hematite.

A promising technique to help improve the efficiency of photovoltaics and photocatalysts is the addition of plasmonic nanoparticles, which have been shown to enhance the efficiency of solar energy systems. This article focuses on the technical aspects of incorporating plasmonic sources of silver and gold nanoparticles into a solar cell and a water splitting system to enhance their solar energy conversion efficiencies. Characteristics of surface plasmon for light absorption enhancement are discussed first, and applications in solar energy conversion and challenges of silver and gold nanostructures in the two energy conversion systems are subsequently discussed.



## Surface Plasmon Resonance of Metallic Nanostructures

Surface plasmon resonance refers to the collective oscillating motion of conduction electrons near a metal surface in an external electromagnetic field and can be excited on metallic nanoparticles, such as silver and gold. The extinction spectra of metallic nanoparticles are usually dominated by one or more well-resolved peaks, which are caused by strong light scattering and absorption. Plasmon resonance frequency is determined by the dispersion relation of the metal, particle size and shape, and the changes in dielectric constant of the surrounding medium. Coupling between individual particles and their geometry can also dramatically influence the position of the plasmon resonance.<sup>19</sup> Surface plasmons of silver and gold nanostructures (Aldrich Prod. Nos. 576832 and 636347) can cause significant enhancement in the local electromagnetic field due to the intense surface plasmon resonance cross-section.<sup>20</sup> Coupling between two or more silver (or gold) nanoparticles can have their excited states localized between the particles and produces even higher local field intensity than the individual nanoparticles.<sup>21</sup> Such field enhancement is expected to increase the light absorption of the photoactive layers of photocatalysts for renewable energy conversion.

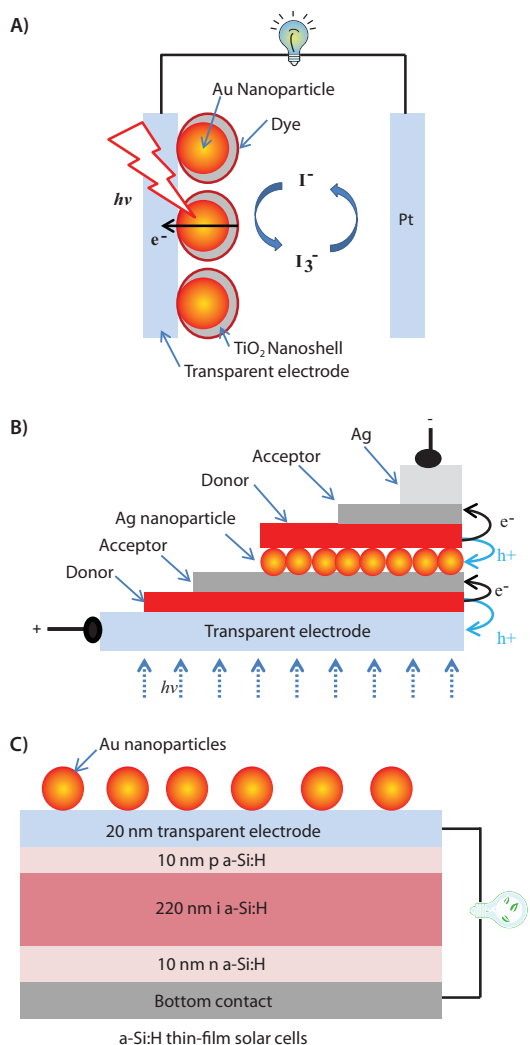


**Figure 1.** Schematic of surface-enhanced dye-sensitized solar cell (A), double heterojunction OPV (B), and silicon solar cell (C) with their efficiencies enhanced by gold nanoparticles.

## Surface-enhanced Solar Energy Conversion Systems

Experimental evidence in the literature has shown that the power efficiency of both solar cells and photocatalytic thin-film electrodes can be enhanced in the presence of metallic nanoparticles because of their surface plasmonic effects. In the field of solar cells, gold nanoparticles have been used to enhance the efficiency of a dye-sensitized solar cell,<sup>22</sup> an organic solar cell,<sup>23</sup> and a silicon solar cell,<sup>24</sup> as shown in **Figure 1**. Gold or silver nanoparticles have been incorporated into these three types of solar cells in such a way that the photoactive layers of the cells benefit from the enhanced light absorption near the plasmonic structure. For example, gold nanoparticles are embedded in a thin layer of TiO<sub>2</sub> under the dye layer in order to enhance the absorption cross-section of the dye-sensitized solar cell (**Figure 1A**). The top coating of gold nanoparticles with TiO<sub>2</sub> is critical to prevent corrosion of gold nanoparticles in the presence of liquid electrolytes. Meanwhile, the thickness control of TiO<sub>2</sub> is very important to allow efficient field enhancement, as plasmon enhancement of the dye layer decreases when it is placed further away from the metallic surface. Recent work on surface plasmon-enhanced organic solid solar cells and relevant organic electronics have been summarized in a recent review article by Rothberg and Pan.<sup>25</sup> Typically, efficiency of a tandem organic solid solar cell with double heterojunctions as shown in **Figure 1B** can be greatly enhanced by silver nanoparticles. To obtain optical light absorption enhancement, the photoactive layers of this device have to be close to the silver nanoparticle surface. Silver nanoparticles in this type of device can also function as charge recombination sites for electrons and holes from each of the two heterojunction cells to help conduct electricity through the double layer junction device. Direct surface coating with gold nanoparticles onto silicon solar cells is also found to improve the device performance by expanding its solar energy response wavelength range and light absorption cross-section (**Figure 1C**). Such top configuration does not interrupt the charge separation and transport of the photoactive layer in the device while enhancing its light absorption, yielding improved device performance.

In the field of direct water splitting, numerous recent studies have shown that enhanced visible light photoelectrochemical response can be observed for thin-film photoanode electrodes by incorporating silver and gold nanoparticles into the electrode (**Figure 2**). Yet, some studies show plasmon sources produce no effect or a decrease in photoelectrochemical efficiency. For example, Thimsen and coworkers<sup>26</sup> show the effects of bare spherical gold particles on the photocatalytic performance of  $\alpha$ -Fe<sub>2</sub>O<sub>3</sub> electrodes with the gold nanoparticles embedded in the hematite layer and on its surface. The embedded gold nanoparticle configuration was found to have no effect on hematite performance; whereas the top configuration on hematite nanoplatelets showed plasmon effect on the photocurrent response. The overall power efficiency decreased in the presence of gold nanoparticles. More recently, Thomann et al.<sup>27</sup> reported bare spherical gold nanoparticles decrease the photocatalytic behavior of  $\alpha$ -Fe<sub>2</sub>O<sub>3</sub> in both embedded and top configurations because gold can serve as a charge recombination center, whereas silica shell-coated gold nanoparticles can enhance photocatalytic efficiency because the charge recombination at gold

nanoparticles is blocked by silica. In addition, different enhancement action spectra were observed for embedded and top configurations due to the changes in electronic structure and morphology of hematite at the solid-liquid interface in the presence of silica-coated gold nanoparticles. Using another approach, Gao and coworkers<sup>28</sup> showed an enhanced photocurrent in a thin-film iron oxide photoanode coated on gold nanopillars. The enhancement factor from 500 nm to 700 nm, corresponding to surface plasmon absorption enhancement, is very small. Despite disagreements in the literature, new cell configurations to incorporate plasmonic nanoparticles into the catalytic layer, based on their size, shape, and surface coverage, and the thickness control of the photocatalytic layer, are critical for improved control of the surface enhancement renewable energy conversion process.

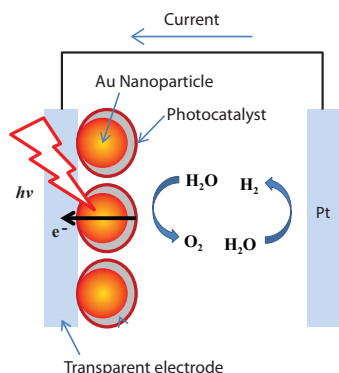


**Figure 2.** Surface-enhanced photoelectrochemical cell for hydrogen generation from direct water splitting using solar energy.

## Conclusions

Silver and gold nanoparticles have been used in thin-film solar cells and photoelectrochemical water splitting systems to enhance their power efficiency. Wavelength dependence of photocurrent or catalytic performance should be taken into account to confirm the plasmonic effect. To avoid formation of charge traps or charge recombination sites in the presence of metallic nanoparticles, surface encapsulation is necessary. This prevents charge flow to the plasmonic antenna system when its surface enhancement capability is used to benefit the energy conversion process. Distance from the photocatalytic layer for direct water splitting or from the photoactive layer of a solar cell should be precisely controlled to optimize the surface enhancement capability. Particle size and density studies are needed to determine the wavelength range where the surface enhancement would benefit from surface plasmon enhancement.

## Acknowledgment

This material is supported by the National Science Foundation under award number CHE-1153120 and the University of Alabama 2010 RGC award.

## References

- O'Regan, B.; Grätzel, M., *Nature*, **1991**, 353, 737-740.
- Zhang, Q. F.; Dandeneau, C. S.; Zhou, X. Y.; Cao, G.Z. *Adv. Mater.* **2009**, 21(41), 4087-4108
- Tang, C. W., *Appl. Phys. Lett.* **1986**, 48(2), 183-185.
- Yang, F.; Sun, K.; Forrest, S. R. *Adv. Mater.* **2007**, 19, 4166-4171.
- Forrest, S. R., *MRS Bull.* **2005**, 30(1), 28-32.
- Sivula, K.; Formal, F. Le; Grätzel, M., *Chem. Mater.*, **2009**, 21, 2862-2867
- Fujishima A.; Honda, K., *Nature*, **1972**, 238, 37-38.
- Grimes, C. A.; Varghese, O. K.; Ranjan, S., *Springer*, **2008**.
- Maeda, K.; Domen, K., *J. Phys. Chem. C*, **2007**, 111, 7851-7861.
- Tafen, D. N.; Wang, J.; Wu, N.; Lewis, J. P., *Appl. Phys. Lett.* **2009**, 94, 093101/1-093101/3.
- Wu, P.; Xie, R.; Shang, J. K., *J. Am. Chem. Soc.* **2008**, 91, 2957-2962.
- Murphy, A. B.; Barnes, P. R. F.; Randeniya, L. K.; Plumb, I. C.; Grey, I. E.; Horne, M. D., Glasscock, J. A. *Int. J. Hydrogen Energy*, **2006**, 31, 1999-2017.
- Inglar, W. B., Jr.; Khan, S. U. M., *Electrochem. Solid-State Lett.*, **2006**, 9, G144-G146
- Wang, H.L.; Deutsch, T.; Turner, J. A., *J. Electrochem. Soc.*, **2008**, 155, F91-F96
- Balberg, I.; Pinch, H. L., *J. Magn. Magn. Mater.* **1978**, 7, 12-15.
- Kennedy, J. H.; Frese, K. W. *J. Electrochem. Soc.* **1978**, 125, 709-714.
- John H. K.; Karl W. F. Jr., *J. Electrochem. Soc.* **1978**, 125, 723-726.
- Kay, A.; Cesar, I.; Grätzel, M. *J. Am. Chem. Soc.* **2006**, 128, 15714-15721.
- Liz-Marzan, L. M., *Langmuir*, **2006**, 22, 32-41.
- Brust, L., *Acc. Chem. Res.* **2008**, 41, 1742-1749.
- Liz-Marzan, Luis M., *Langmuir*, **2006**, 22, 32-41.
- Schatz, G. S.; Hupp, J. T.; Standridge, S. D. *J. Am. Chem. Soc.* **2009**, 131, 8407-8409.
- Yakimov, A.; Forrest, S. R., *Appl. Phys. Lett.* **2002**, 80, 1667-1669.
- Derkacs, D.; Lim, S. H.; Matheu, P.; Mar W., Yu, E. T., *Appl. Phys. Lett.*, **2006**, 89, 0931031-3.
- Rothberg, L. J.; Pan, S. L., "Surface enhanced photoluminescence and applicant in organic electronics" in *Metal-Enhanced Fluorescence*, Editor, Chris D. Geddes, **2010** John Wiley & Sons, Inc.
- Thimsen, E.; Le Formal, F.; Grätzel, M.; Warren, S. C. *Nano Lett.* **2011**, 11, 35-43.
- Thomann, I.; Pinaud, B. A.; Chen, Z.; Clemens, B. M.; Jaramillo, T. F.; Brongersma, M. L. *Nano Lett.* **2011**, 11, 3440-3446.
- Gao, H.; Liu, C.; Jeong, H. E.; Yang, P. *ACS Nano* **2012**, 6, 234-240.

## Iron (III) Oxide (Fe<sub>2</sub>O<sub>3</sub>) Materials

For a complete list of available materials, visit [aldrich.com/periodic](http://aldrich.com/periodic).

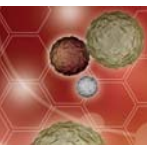
For a complete list of available iron oxide deposition precursors, visit [aldrich.com/deposition](http://aldrich.com/deposition).

Name	Purity	Particle Size	Form	Prod. No.
Iron(III) oxide, dispersion	20 wt. % in ethanol	avg. part. size <30 nm (APS) particle size <110 nm (DLS)	nanoparticles	<a href="#">720712-100G</a>
Iron(III) oxide, dispersion	20 wt. % in H <sub>2</sub> O	avg. part. size <30 nm (APS) particle size <100 nm (DLS)	nanoparticles	<a href="#">720704-100G</a>
Iron nickel oxide	≥98% trace metals basis	particle size <50 nm	nanopowder	<a href="#">637149-25G</a> <a href="#">637149-100G</a>
Iron(III) oxide	-	particle size <50 nm	nanopowder	<a href="#">544884-5G</a> <a href="#">544884-25G</a>
Iron(III) oxide	99.999% trace metals basis	-	powder	<a href="#">529311-5G</a> <a href="#">529311-25G</a>
Iron(III) oxide	99.8% trace metals basis	3 - 12 mm	pieces sintered	<a href="#">343005-50G</a> <a href="#">343005-250G</a>
Iron(III) oxide	≥99%	<5 μm	powder	<a href="#">310050-25G</a> <a href="#">310050-500G</a> <a href="#">310050-2.5KG</a>
Iron(III) oxide	99.98% trace metals basis	-	powder and chunks	<a href="#">203513-10G</a> <a href="#">203513-50G</a>
Iron(III) oxide	≥99.0%, RT	-	-	<a href="#">44956-100G</a>

## Silver Nanoparticles

For a complete list of available materials, visit [aldrich.com/nanosilver](http://aldrich.com/nanosilver).

Name	Concentration	Particle Size	Stabilizer	Form	Prod. No.
Silver nanowires	0.5% in isopropanol (suspension)	diam. × L 115 nm × 30 μm	-	liquid (suspension)	<a href="#">739448-25ML</a>
Silver nanowires	0.5% in isopropanol (suspension)	diam. × L 60 nm × 10 μm	-	liquid (suspension)	<a href="#">739421-25ML</a>
Silver, dispersion	0.02 mg/mL in aqueous buffer 0.02 mg/mL ±5% (mass)	average diameter 60 nm ±4 nm (TEM) particle size 60 nm (TEM)	sodium citrate	nanoparticles	<a href="#">730815-25ML</a>
Silver, dispersion	0.02 mg/mL ±5% (mass) 0.02 mg/mL in aqueous buffer	average diameter 40 nm ±4 nm (TEM) particle size 40 nm (TEM)	sodium citrate	nanoparticles	<a href="#">730807-25ML</a>
Silver, dispersion	0.02 mg/mL ±5% (mass) 0.02 mg/mL in aqueous buffer	average diameter 20 nm ±4 nm (TEM) particle size 20 nm (TEM)	sodium citrate	nanoparticles	<a href="#">730793-25ML</a>
Silver, dispersion	0.02 mg/mL ±5% (mass) 0.02 mg/mL in aqueous buffer	average diameter 10 nm ±4 nm (TEM) particle size 10 nm (TEM)	sodium citrate	nanoparticles	<a href="#">730785-25ML</a>
Silver, dispersion	0.02 mg/mL in aqueous buffer 0.02 mg/mL ±5%	average diameter 100 nm ±7 nm (TEM) particle size 100 nm (TEM)	sodium citrate	nanoparticles	<a href="#">730777-25ML</a>
Silver, dispersion	0.25 mM in H <sub>2</sub> O	particle size ~157 nm	citrate	dispersion nanoparticles	<a href="#">675318-5ML</a>
Silver	-	particle size <150 nm	-	nanopowder	<a href="#">484059-5G</a>
Silver	-	particle size <100 nm	-	nanopowder	<a href="#">576832-5G</a>



## One-dimensional Gold Nanostructures Stabilized in CTAB

For a complete list of available materials, visit [aldrich.com/nanomaterials](http://aldrich.com/nanomaterials).

Name	Concentration	Dimensions	Form	Prod. No.
Gold nanorods	> 30 µg/mL	diameter 10 nm	colloidal suspension dispersion in H <sub>2</sub> O	716812-25ML
Gold nanorods	> 30 µg/mL	diameter 10 nm	colloidal suspension dispersion in H <sub>2</sub> O	716820-25ML
Gold nanorods	> 30 µg/mL	diameter 10 nm	colloidal suspension dispersion in H <sub>2</sub> O	716839-25ML
Gold nanorods	> 45 µg/mL	diam. × L 25 × 60 nm	colloidal suspension dispersion in H <sub>2</sub> O	771686-25ML
Gold nanorods	> 45 µg/mL	diam. × L 25 × 47 nm	colloidal suspension dispersion in H <sub>2</sub> O	771651-25ML
Gold nanorods	> 45 µg/mL	diam. × L 25 mm × 34 nm	colloidal suspension dispersion in H <sub>2</sub> O	771643-25ML
Gold nanowires	≥ 50 µg/mL 60 µg/mL in H <sub>2</sub> O	diam. × L 30 × 4,500 nm	dispersion (H <sub>2</sub> O)	716944-10ML
Gold nanowires	> 50 µg/mL	diam. × L 30 × 6,000 nm	dispersion (H <sub>2</sub> O)	716952-10ML
Gold microrods	> 50 µg/mL 50 µg/mL in H <sub>2</sub> O	diam. × L 200 × 1,000 nm	colloidal suspension dispersion (H <sub>2</sub> O)	716960-10ML

## Gold Nanoparticles Stabilized in Citrate

For a complete list of available materials, visit [aldrich.com/nanomaterials](http://aldrich.com/nanomaterials).

Name	Concentration	Particle Size	Prod. No.
Gold nanoparticles	~ 5.5E+13 particles/mL	diameter 5 nm	741949-25ML 741949-100ML
Gold nanoparticles	~ 6.0E+12 particles/mL	diameter 10 nm	741957-25ML 741957-100ML
Gold nanoparticles	~ 7.2E+11 particles/mL	diameter 20 nm	741965-25ML 741965-100ML
Gold nanoparticles	~ 1.8E+11 particles/mL	diameter 30 nm	741973-25ML 741973-100ML
Gold nanoparticles	~ 7.2E+10 particles/mL	diameter 40 nm	741981-25ML 741981-100ML
Gold nanoparticles	~ 3.5E+10 particles/mL	diameter 50 nm	742007-25ML 742007-100ML
Gold nanoparticles	~ 1.9E+10 particles/mL	diameter 60 nm	742015-25ML 742015-100ML
Gold nanoparticles	~ 7.8E+9 particles/mL	diameter 80 nm	742023-25ML 742023-100ML
Gold nanoparticles	~ 3.8E+9 particles/mL	diameter 100 nm	742031-25ML 742031-100ML
Gold nanoparticles	~ 3.6E+9 particles/mL	diameter 150 nm	742058-25ML 742058-100ML
Gold nanoparticles	~ 1.9E+9 particles/mL	diameter 200 nm	742066-25ML 742066-100ML
Gold nanoparticles	~ 7.1E+8 particles/mL	diameter 250 nm	742074-25ML 742074-100ML
Gold nanoparticles	~ 4.5E+8 particles/mL	diameter 300 nm	742082-25ML
Gold nanoparticles	~ 1.9E+8 particles/mL	diameter 400 nm	742090-25ML
Gold	-	particle size <100 nm	636347-1G

## Gold Nanoparticles Stabilized in PBS

For a complete list of available materials, visit [aldrich.com/nanomaterials](http://aldrich.com/nanomaterials).

Name	Concentration	Particle Size	Prod. No.
Gold nanoparticles	~ 5.5E+13 particles/mL	diameter 5 nm	752568-25ML 752568-100ML
Gold nanoparticles	~ 6.0E+12 particles/mL	diameter 10 nm	752584-25ML 752584-100ML
Gold nanoparticles	~ 7.2E+11 particles/mL	diameter 20 nm	753610-25ML 753610-100ML
Gold nanoparticles	~ 1.8E+11 particles/mL	diameter 30 nm	753629-25ML 753629-100ML
Gold nanoparticles	~ 7.2E+10 particles/mL	diameter 40 nm	753637-25ML 753637-100ML



Name	Concentration	Particle Size	Prod. No.
Gold nanoparticles	~ 3.5E+10 particles/mL	diameter 50 nm	753645-25ML 753645-100ML
Gold nanoparticles	~ 1.9E+10 particles/mL	diameter 60 nm	753653-25ML 753653-100ML
Gold nanoparticles	~ 7.8E+9 particles/mL	diameter 80 nm	753661-25ML 753661-100ML
Gold nanoparticles	~ 3.8E+9 particles/mL	diameter 100 nm	753688-25ML 753688-100ML

## Precursors for TiO<sub>2</sub> Films

For a complete list of available materials, visit [aldrich.com/mnel](http://aldrich.com/mnel).

Name	Linear Formula	Purity	Form	Prod. No.
Tetrakis(dimethylamido)titanium(IV)	$[(CH_3)_2N]_4Ti$	99.999%	liquid	469858-5G 469858-25G
Tetrakis(diethylamido)titanium(IV)	$[(C_2H_5)_2N]_4Ti$	99.999% trace metals basis	liquid	469866-5G 469866-25G
Tetrakis(ethylmethylamido)titanium(IV)	$[(CH_3C_2H_5)N]_4Ti$	≥99.99%	liquid	473537-5G
Titanium(IV) diisopropoxidebis(2,2,6,6-tetramethyl-3,5-heptanedionate)	$Ti[OC(C_2H_5)_2CH_2OC(C_2H_5)_2(C_2H_5)_2(C_2H_5)_2]_2$	99.99%	solid	494143-5G
Bis(diethylamido)bis(dimethylamido)titanium(IV)	$Ti(N(CH_3)_2)_2(N(C_2H_5)_2)_2$	≥95% ≥99.99% trace metals basis	liquid	J100026-10G

## TiO<sub>2</sub> Sol-Gel Precursors

For a complete list of available materials, visit [aldrich.com/mnel](http://aldrich.com/mnel).

Name	Linear Formula	Purity	Form	Prod. No.
Titanium(IV) isopropoxide	$Ti[OCH(CH_3)_2]_4$	97%	liquid	205273-4X25ML 205273-100ML 205273-500ML 205273-2L
Titanium(IV) butoxide	$Ti(OCH_2CH_2CH_2CH_3)_4$	97%	liquid (or viscous liquid)	244112-5G 244112-100G 244112-500G 244112-2KG
Chlorotrisisopropoxytitanium(IV)	$[(CH_3)_2CHO]_3TiCl$	95%	liquid	250627-100G 250627-800G
Chlorotrisisopropoxytitanium(IV) solution	$[(CH_3)_2CHO]_3TiCl$	-	solution, 1.0 M in hexanes	252670-100ML
Titanium(IV) propoxide	$Ti(OC_3H_7)_4$	98%	liquid	253081-100G 253081-500G
Titanium(IV) oxyacetylacetonate	$Ti[OCH_2COCH=C(O)CH_3]_2$	90%	powder	330833-10G 330833-50G
Titanium(IV) 2-ethylhexyloxide	$Ti[OCH_2CH(C_2H_5)(CH_2)_3CH_3]_4$	95%	liquid	333484-5ML 333484-250ML
Titanium(IV) isopropoxide	$Ti[OCH(CH_3)_2]_4$	99.999% trace metals basis	liquid liquid	377996-5ML 377996-25ML 377996-100ML
Titanium(IV) methoxide	$Ti(OCH_3)_4$	≥99.99% trace metals basis	powder	463582-25G
Titanium(IV) methoxide	$Ti(OCH_3)_4$	95%	solid	404950-10G 404950-50G
Titanium(IV) butoxide	$Ti(OCH_2CH_2CH_2CH_3)_4$	≥97.0%, gravimetric	liquid	86910-250ML 86910-1L
Titanium(IV) ethoxide	$Ti(OC_2H_5)_4$	-	liquid	244759-50G 244759-250G
Titanium diisopropoxide bis(acetylacetonate)	$[(CH_3)_2CHO]_2Ti(C_5H_7O_2)_2$	-	solution	325252-100ML 325252-500ML
Titanium(IV) <i>tert</i> -butoxide	$Ti[OC(CH_3)_3]_4$	-	liquid	462551-25ML 462551-50ML

# Materials for Clean H<sub>2</sub> Production from Bioethanol Reforming



Hong Xie, Eric Weitz, and Kenneth R. Poepelmeier\*  
Center for Catalysis and Surface Science, Department of Chemistry  
Northwestern University  
2145 Sheridan Road, Evanston, Illinois 60208  
\*krp@northwestern.edu

## Introduction

Hydrogen is one of the most important resources in providing food, fuel, and chemical products for our everyday life. Sustainable catalytic hydrogen production from bioethanol has gained significant attention in recent years due to globally diminishing fossil fuel supplies, which have necessitated the search for new chemical feedstocks. Ethanol has been considered as one of the most promising renewable energy resources since it has low toxicity and can be safely stored and easily transported. Bioethanol is the ethanol produced by fermentation of biomass materials including sugar cane, corn, and lignocellulose. Catalytic steam reforming (SR) of ethanol has been extensively investigated for hydrogen production in the past decade. These SR reactions are commonly carried out using heterogeneous catalysts, which include an active phase of nanosized metal particles on an oxide support. This article reviews the catalytic process for bioethanol reforming with a focus on supported nanoscale rhodium catalysts.

## Thermodynamics for Ethanol Steam Reforming (SR)

The overall SR of ethanol can be simplified as:  $C_2H_5OH + 3H_2O \rightarrow 6H_2 + 2CO_2$ . A typical reaction mechanism for ethanol SR reaction is presented in **Figure 1**. Ethanol conversion by SR may include<sup>1-3</sup>:

1. ethanol dehydrogenation to form acetaldehyde
2. acetaldehyde decarbonylation to produce CH<sub>4</sub> and CO
3. CH<sub>4</sub> reforming, i.e.,  $CH_4 + H_2O \rightarrow CO + 3H_2$
4. the production of H<sub>2</sub> through a water-gas-shift (WGS) reaction:  $CO + H_2O \rightarrow CO_2 + H_2$ .

The goal for the SR process is to obtain a high yield of H<sub>2</sub> and a high selectivity toward CO<sub>2</sub>, since a total of 6 moles of H<sub>2</sub> can be obtained from ethanol for every 2 moles of CO<sub>2</sub> produced. The CO generated in the SR process is undesired, as it can be poisonous to the catalysts or the electrode in fuel cell applications. Therefore, the demand of high CO<sub>2</sub> selectivity makes it necessary to couple SR reaction with WGS reaction.

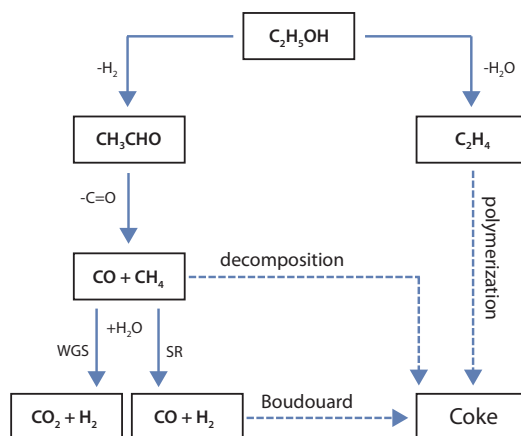


**Figure 1.** Reaction mechanism scheme of ethanol steam reforming.

Depending on the catalysts and reaction conditions, the actual ethanol SR reaction may undergo different reaction pathways such as ethanol dehydration and decomposition pathways to generate undesired by-products of CO, CH<sub>4</sub>, and C<sub>2</sub>H<sub>4</sub>, etc. that may lead to coke formation and consequently lower H<sub>2</sub> production. The main reactions that may contribute to coke formation are: ethanol dehydration to ethylene followed by polymerization to coke; Boudouard reaction, i.e., carbon monoxide decomposition to form carbon dioxide and coke; and methane decomposition to form coke and hydrogen. In addition, catalyst sintering under SR reaction conditions can also lead to deteriorated catalytic performance by increasing the active phase particle sizes and decreasing the amount of available surface active sites.

Catalysts play a decisive role in the reaction stability, ethanol conversion, and H<sub>2</sub> selectivity for ethanol SR reactions. It is, therefore, crucial to develop suitable catalysts that will maximize H<sub>2</sub> yield, and inhibit CO production and coke formation that will deactivate catalysts.

## Rh-supported Catalysts

Supported transition metal catalysts such as Co and Ni catalysts have been investigated for ethanol reforming reactions.<sup>4-6</sup> However, compared to transition metal catalysts, supported noble metal catalysts have shown greatly enhanced performance at much lower metal loadings for the SR of ethanol (**Table 1**). Aupretre et al.<sup>7</sup> investigated the catalytic performance of  $\gamma$ -Al<sub>2</sub>O<sub>3</sub> supported Rh, Pt, Pd, and Ru catalysts with metal loadings of 0.67–1 wt% for the ethanol SR reaction at 700 °C. The 1 wt% Rh catalyst proved to be the most active and selective of these noble metals. Breen et al.<sup>8</sup> also reported that Rh/Al<sub>2</sub>O<sub>3</sub> (**Aldrich Prod. No. 212857**) showed a higher ethanol conversion than Al<sub>2</sub>O<sub>3</sub> (**Aldrich Prod. No. 202606**) supported Pd, Pt, and Ni catalysts under the same reaction conditions from 400–700 °C. Frusteri et al.<sup>1</sup> studied MgO (**Aldrich Prod. No. 529699**) supported Rh, Pd, Ni, and Co catalysts in the SR of simulated bioethanol at 650 °C. Again, the Rh/MgO showed the best performance in terms of reaction activity and stability. Furthermore, the Rh/MgO catalyst was most resistant to coke formation and metal sintering. In contrast, Ni, Co and Pd catalysts deactivated mainly due to metal sintering. Rioche<sup>9</sup> et al. reported the SR of ethanol from 664–779 °C over Pt, Pd and Rh catalysts supported on Al<sub>2</sub>O<sub>3</sub> and CeZrO<sub>2</sub> (**Aldrich Prod. No. 634174**). Only the Rh-based catalysts efficiently converted the ethanol over the temperature range investigated. The Pt- and Pd-based catalysts were significantly less active.



The high SR reaction activity of the Rh catalysts is due to the fact that Rh favors C–C bond cleavage compared to other noble metals. Duprez et al.<sup>7</sup> proposed a bi-functional mechanism where the hydrocarbon would be activated on the metal phase while the water molecule would be activated on the support as hydroxyl groups. Owing to this effect, oxide supports with enhanced surface oxygen mobility are expected to have improved SR reaction activity.

## Support Effects

As shown in **Table 1**, rhodium is the most active metal for ethanol SR. However, the support also plays a significant role in determining the catalytic performance of the catalysts for ethanol SR reaction (**Table 2**). The use of CeO<sub>2</sub>–ZrO<sub>2</sub>, a redox mixed oxide, led to higher H<sub>2</sub> yields as compared to the Al<sub>2</sub>O<sub>3</sub>-supported catalysts.<sup>9</sup> Roh et al.<sup>10</sup> studied Rh catalysts on various supports, including Al<sub>2</sub>O<sub>3</sub>, MgAl<sub>2</sub>O<sub>4</sub> (**Aldrich Prod. No. 677396**), ZrO<sub>2</sub> (**Aldrich Prod. No. 204994**), and ZrO<sub>2</sub>–CeO<sub>2</sub> for ethanol SR reaction. For the 1 wt% Rh catalysts, at temperatures ≤450 °C, the reaction activity was found to decrease in the order: Rh/ZrO<sub>2</sub>–CeO<sub>2</sub> > Rh/Al<sub>2</sub>O<sub>3</sub> > Rh/MgAl<sub>2</sub>O<sub>4</sub> > Rh/ZrO<sub>2</sub>. The 1% Rh/ZrO<sub>2</sub>–CeO<sub>2</sub> catalyst exhibited the highest CO<sub>2</sub> selectivity up to 550 °C. At 450 °C, the CO<sub>2</sub> selectivity of 52% was at least 3 times higher than all other tested catalysts. Furthermore, the 1% Rh/ZrO<sub>2</sub>–CeO<sub>2</sub> catalyst exhibited the highest H<sub>2</sub> yield among all the catalysts at temperatures below 500 °C.

Generally, a good SR catalyst support should favor Rh stability with minimum Rh sintering. In addition, water should be activated on the support as mobile surface hydroxyl groups to promote reaction with CH<sub>x</sub>O<sub>y</sub> fragments adsorbed on Rh species. Finally, it should favor ethanol dehydrogenation to acetaldehyde instead of ethanol dehydration to ethylene in order to prevent coke formation. In fact, the acidic Al<sub>2</sub>O<sub>3</sub> support is very active for the dehydration reaction leading to the formation of ethylene,<sup>8</sup> which is undesirable in ethanol SR. Over a CeO<sub>2</sub> support, acetaldehyde can be formed via the dehydrogenation of ethanol.<sup>3</sup> CeO<sub>2</sub> (**Aldrich Prod. No. 211575**) can promote the redox reaction of rhodium due to its high oxygen storage capacity associated with the fast Ce<sup>4+</sup>/Ce<sup>3+</sup> redox process.<sup>10</sup> ZrO<sub>2</sub>, with its high thermal stability and tunable acidic and basic properties,<sup>11</sup> has also been used as a catalyst support for ethanol SR reactions. Zhong et al.<sup>12</sup> studied Rh catalysts supported on ZrO<sub>2</sub>-based oxides; in their study, pure ZrO<sub>2</sub> resulted in higher H<sub>2</sub> yield compared to the binary metal oxide supports of ZrO<sub>2</sub> with Al<sub>2</sub>O<sub>3</sub>, La<sub>2</sub>O<sub>3</sub>, or Li<sub>2</sub>O at 300 °C. The addition of ZrO<sub>2</sub> to CeO<sub>2</sub> can enhance the oxygen storage capacity, the reducibility of Ce<sup>4+</sup>, and thermal stability of CeO<sub>2</sub>.<sup>13</sup> It is possible that ZrO<sub>2</sub>–CeO<sub>2</sub> may transfer mobile oxygen species to Rh to enhance CH<sub>4</sub> reforming and subsequent H<sub>2</sub> production, while the oxygen vacancies would be replenished by water molecules from the redox cycle during the SR of ethanol.<sup>7,10</sup> Among the investigated supports, CeO<sub>2</sub>, MgO, and ZrO<sub>2</sub> are the most suitable catalyst supports for effective ethanol SR with Rh catalysts.

**Table 1.** Steam reforming of ethanol using noble metal catalysts

Metal	Loading (%)	Support	Temperature (°C)	Ethanol/Steam (molar ratio)	Ethanol Conversion (%)	H <sub>2</sub> Yield (%)	Selectivity (CO <sub>2</sub> , %)	Reference No.
Rh	3	MgO	650	1:8.5	16.5		67.1	(1)
Pd	3	MgO	650	1:8.5	6.8		32.8	
Co	20	MgO	650	1:8.5	19		44.4	
Ni	20	MgO	650	1:8.5	10.4		58.2	(7)
Rh	1	γ-Al <sub>2</sub> O <sub>3</sub>	700	1:3		2.3 <sup>A</sup>	75	
Pt	1	γ-Al <sub>2</sub> O <sub>3</sub>	700	1:3		0.6	35	
Pd	0.75	γ-Al <sub>2</sub> O <sub>3</sub>	700	1:3		1.1	10	(8)
Ru	0.67	γ-Al <sub>2</sub> O <sub>3</sub>	700	1:3		0.3	18	
Rh	1	Al <sub>2</sub> O <sub>3</sub>	650	1:3	88 <sup>B</sup>			
Pt	1	Al <sub>2</sub> O <sub>3</sub>	650	1:3	26			(9)
Pd	0.5	Al <sub>2</sub> O <sub>3</sub>	650	1:3	17			
Ni	5	Al <sub>2</sub> O <sub>3</sub>	650	1:3	5			
Rh	1	CeZrO <sub>2</sub>	686	1:3		78	22 <sup>C</sup>	(9)
Pt	1	CeZrO <sub>2</sub>	684	1:3		43	20	
Pd	1	CeZrO <sub>2</sub>	676	1:3		6	1	

A. H<sub>2</sub> yield (g h<sup>-1</sup> g<sup>-1</sup> catalyst)

B. Ethanol conversion based on CO + CO<sub>2</sub> formation

C. CO<sub>2</sub> yield

**Table 2.** Steam reforming of ethanol using 1 wt% Rh catalysts on different supports

Support	Temperature (°C)	Ethanol/Steam (molar ratio)	Ethanol Conversion (%)	H <sub>2</sub> Yield (%)	Selectivity (CO <sub>2</sub> , %)	Reference No.
CeZrO <sub>2</sub>	779	1:3		80	17.5 <sup>B</sup>	(9)
Al <sub>2</sub> O <sub>3</sub>	777	1:3		67	16.5	
ZrO <sub>2</sub> –CeO <sub>2</sub>	450	1:8	100	3.5 <sup>A</sup>	52	(11)
Al <sub>2</sub> O <sub>3</sub>	450	1:8	96	1.2	1.2	
MgAl <sub>2</sub> O <sub>4</sub>	450	1:8	75	1.7	10	
ZrO <sub>2</sub>	450	1:8	42	1.5	12	(13)
ZrO <sub>2</sub>	300	1:10		4.0 <sup>A</sup>		
ZrO <sub>2</sub> –La <sub>2</sub> O <sub>3</sub> <sup>C</sup>	300	1:10		2.4		
ZrO <sub>2</sub> –Al <sub>2</sub> O <sub>3</sub> <sup>D</sup>	300	1:10		3.2		

A. H<sub>2</sub> produced/ethanol feed (mol/mol)

B. CO<sub>2</sub> yield

C. 99 wt% ZrO<sub>2</sub> + 1 wt% La<sub>2</sub>O<sub>3</sub>

D. 99 wt% ZrO<sub>2</sub> + 1 wt% Al<sub>2</sub>O<sub>3</sub>

## Preparation Method Effects

The catalyst preparation methods can also affect the catalytic performance of the resulting catalysts. Aupretre et al.<sup>14</sup> prepared a MgAl<sub>2</sub>O<sub>4</sub> spinel support by solid-solid reaction between MgO and Al<sub>2</sub>O<sub>3</sub>. Compared with the Al<sub>2</sub>O<sub>3</sub>-supported catalysts, the spinel-supported catalysts exhibited a slightly higher basicity; whereas the surface acidity was strongly reduced. The MgAl<sub>2</sub>O<sub>4</sub> was impregnated with different Rh precursor salts (nitrate, chloride, acetate) to obtain the supported Rh catalysts, which gave less acidic catalysts with greatly enhanced ethanol SR performances compared with the Rh catalysts supported on Mg<sub>x</sub>Ni<sub>1-x</sub>Al<sub>2</sub>O<sub>4</sub>/Al<sub>2</sub>O<sub>3</sub>. In this case, the Rh precursor salts had a substantial impact on the properties of the final catalysts. The use of a Rh nitrate precursor dramatically increased the overall acidity of the catalyst, while a Rh acetate precursor gave the catalyst with lowest acidity. Rh chloride resulted in catalysts with moderate acidity, allowing the preparation of well-dispersed Rh catalysts that were very active and stable for ethanol SR. Zhong et al.<sup>12</sup> prepared ZrO<sub>2</sub> supports using a co-precipitation method (ZrO<sub>2</sub>-CP) and a hydrothermal method (ZrO<sub>2</sub>-HT). A significant enhancement in catalytic activity, selectivity, and stability was achieved by the ZrO<sub>2</sub>-HT-supported Rh catalyst compared with its ZrO<sub>2</sub>-CP-supported counterpart at temperatures below 400 °C. Relatively strong Lewis acidic sites were found on the Rh/ZrO<sub>2</sub>-HT catalyst, which was responsible for the strong absorption of ethanol and the subsequent C-H cleavage. In contrast, on the Rh/ZrO<sub>2</sub>-CP catalyst, the ethanol adsorption was weak and the C-C cleavage was the dominating reaction. Recent studies<sup>15</sup> have shown the effectiveness of the HT approach coupled with an optimized calcination treatment on the preparation of a nanosized, hydrothermally stable ZrO<sub>2</sub> support of less than 20 nm (Figure 2). Pt deposited on this ZrO<sub>2</sub> support showed enhanced activity for WGS reaction compared to a series of commercial ZrO<sub>2</sub>-supported Pt catalysts. This ZrO<sub>2</sub> support may have great potential in bioethanol SR application.

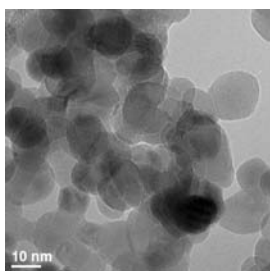


**Figure 2.** TEM image of ZrO<sub>2</sub>. ZrO<sub>2</sub> was prepared using the HT synthesis method coupled with optimized calcination.

## Promoter Effects

The introduction of alkali or alkali earth metal species into the supported Rh catalysts can improve the catalyst stability and performance. Roh et al.<sup>16</sup> studied the deactivation of Rh/CeO<sub>2</sub>-ZrO<sub>2</sub> catalysts for ethanol SR at 350 °C with a high space velocity of 480,000 cm<sup>3</sup>/g·h. Ethanol conversion decreased from 70% to 6% within 5 h due to coke deposition. The addition of 0.5% potassium increased the catalyst stability at the same reaction temperature of 350 °C. Chen et al.<sup>17</sup> introduced Ca to neutralize the acidity of Al<sub>2</sub>O<sub>3</sub>, which helped decrease the undesired reaction pathway of the ethanol dehydration. Furthermore, the addition of Fe into this Ca-Al<sub>2</sub>O<sub>3</sub>-supported Rh catalyst allowed the transfer of CO from Rh to Fe species for subsequent WGS reaction to produce CO-free H<sub>2</sub>, which improved the Rh catalyst stability. Indeed, the acidic and basic properties of the supports strongly affect the SR reaction selectivity toward acetaldehyde and ethylene.<sup>14</sup> Basic sites on the supports benefit the ethanol dehydrogenation step in acetaldehyde formation while the acidic sites need to be neutralized to decrease the ethylene formation.

## Loading Effects

Catalyst loading also affects ethanol SR reaction activity. Roh et al.<sup>10</sup> discovered that, for ethanol SR at 450 °C, the H<sub>2</sub> yield based on per mole of ethanol decreased in the order: 2% Rh/ZrO<sub>2</sub>-CeO<sub>2</sub> > 1% Rh/ZrO<sub>2</sub>-CeO<sub>2</sub> > 3% Rh/ZrO<sub>2</sub>-CeO<sub>2</sub>, possibly due to differences in metal dispersion. Ethanol SR has been more extensively studied over the temperature range 600–700 °C since H<sub>2</sub> selectivity is increased at these high temperatures. Liguas et al.<sup>18</sup> reported the effect of metal loading on catalytic performance over Ru/γ-Al<sub>2</sub>O<sub>3</sub> catalysts. They observed that the ethanol full conversion temperature was 825 °C for the 0.5% Rh catalyst, which was lowered to 775 °C in the case of the 2.0% Rh catalyst. Furthermore, the selectivities toward H<sub>2</sub> and CO<sub>2</sub> were substantially enhanced with increasing Rh loading. Additionally, the 2.0% Rh/Al<sub>2</sub>O<sub>3</sub> catalyst fully converted ethanol without the formation of acetaldehyde or ethylene at temperatures close to 800 °C. The observed differences in catalytic performance were attributed to the increased number of active sites but not the differences in particle sizes with increasing metal loadings, since the rhodium particle sizes were ~2.1 nm for all these Rh/Al<sub>2</sub>O<sub>3</sub> catalysts.

## Conclusions

In the present review, an overview of previous ethanol steam reforming (SR) studies focusing on Rh has been given. Rh has been identified as the most active metal for ethanol SR reaction. Catalyst support, catalyst preparation method, metal additive promoter, and Rh loading all play important roles in optimizing performance of the ethanol SR reaction. The catalyst performance characteristics suggest a strong metal-support interaction. The ethanol SR reaction network is complex and water-gas-shift (WGS) reaction also plays an important role in the overall reforming process. Undesirable reaction pathways such as ethanol dehydration and CH<sub>4</sub> decomposition can lead to coke deposition and, consequently, deactivate the catalyst. The use of a binary support system such as MgO-Al<sub>2</sub>O<sub>3</sub> and CeO<sub>2</sub>-ZrO<sub>2</sub>, and the introduction of hetero-metal species may inhibit carbon deposition leading to better Rh dispersion and, consequently, improve catalyst performance for clean H<sub>2</sub> production from bioethanol. Finally, the introduction of new nanosized hydrothermally prepared catalyst support materials presents a promising avenue toward increased catalytic performance for ethanol SR.

## Acknowledgment

This material is based upon work supported as part of the Institute for Atom-efficient Chemical Transformations (IACT), an Energy Frontier Research Center funded by the U.S. Department of Energy, Office of Science, Office of Basic Energy Sciences.

## References

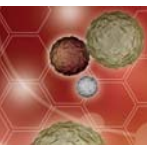
- (1) Frusteri, F.; Freni, S.; Spadaro, L.; Chiodo, V.; Bonura, G.; Donato, S.; Cavallaro, S. *Catalysis Communications* **2004**, *5*, 611.
- (2) Haryanto, A.; Fernando, S.; Murali, N.; Adhikari, S. *Energy Fuels* **2005**, *19*, 2098.
- (3) Ni, M.; Leung, D. Y. C.; Leung, M. K. H. *Int. J. Hydrogen Energy* **2007**, *32*, 3238.
- (4) Llorca, J.; Homs, N. s.; Sales, J.; de la Piscina, P. R. r. *Journal of Catalysis* **2002**, *209*, 306.
- (5) Fatsikostas, A. N.; Kondarides, D. I.; Verykios, X. E. *Catalysis Today* **2002**, *75*, 145.
- (6) Song, H.; Ozkan, U. S. *Journal of Catalysis* **2009**, *261*, 66.

- (7) Aupretre, F.; Descorme, C.; Duprez, D. *Catal. Commun.* **2002**, *3*, 263.
- (8) Breen, J. P.; Burch, R.; Coleman, H. M. *Appl. Catal., B* **2002**, *39*, 65.
- (9) Rioche, C.; Kulkarni, S.; Meunier, F. C.; Breen, J. P.; Burch, R. *Appl. Catal., B* **2005**, *61*, 130.
- (10) Roh, H.-S.; Wang, Y.; King, D. L. *Top. Catal.* **2008**, *49*, 32.
- (11) Yamaguchi, T. *Catal. Today* **1994**, *20*, 199.
- (12) Zhong, Z.; Ang, H.; Choong, C.; Chen, L.; Huang, L.; Lin, J. *Phys. Chem. Chem. Phys.* **2009**, *11*, 872.
- (13) Rossignol, S.; Gerard, F.; Duprez, D. *Journal of Materials Chemistry* **1999**, *9*, 1615.
- (14) Aupretre, F.; Descorme, C.; Duprez, D.; Casanave, D.; Uzio, D. *J. Catal.* **2005**, *233*, 464.
- (15) Xie, H.; Lu, J.; Elam, J. W.; Shekhar, M.; Delgass, W. N.; Ribeiro, F. H.; Weitz, E.; Poepelmeier, K. R. *submitted* **2012**.
- (16) Roh, H.-S.; Platon, A.; Wang, Y.; King, D. L. *Catal. Lett.* **2006**, *110*, 1.
- (17) Chen, L.; Choong, C. K. S.; Zhong, Z.; Huang, L.; Ang, T. P.; Hong, L.; Lin, J. *J. Catal.* **2010**, *276*, 197.
- (18) Liguras, D. K.; Kondarides, D. I.; Verykios, X. E. *Applied Catalysis B: Environmental* **2003**, *43*, 345.

## Nanoscale Catalyst Supports

For a complete list of available materials, visit [aldrich.com/nanomaterials](http://aldrich.com/nanomaterials).

Name	Composition	Purity	Dimensions	Form	Prod. No.
Silica	SiO <sub>2</sub>	99.8% trace metals basis	avg. part. size 12 nm	nanopowder	718483-100G
Aluminum oxide	Al <sub>2</sub> O <sub>3</sub>	99.8% trace metals basis	particle size 13 nm	nanopowder	718475-100G
Titanium(IV) oxide	TiO <sub>2</sub>	≥99.5% trace metals basis	particle size ~21 nm	nanopowder	718467-100G
Aluminum oxide	Al <sub>2</sub> O <sub>3</sub>	20 wt. % in isopropanol	particle size <50 nm (DLS)	nanoparticles	702129-100G 702129-500G
Silicon dioxide, alumina doped	(SiO <sub>2</sub> ) <sub>x</sub> (Al <sub>2</sub> O <sub>3</sub> ) <sub>y</sub>	99.99% trace metals basis 20 wt. % in H <sub>2</sub> O	particle size <50 nm	dispersion nanoparticles	701491-25ML 701491-100ML
Titanium(IV) oxide, mixture of rutile and anatase	TiO <sub>2</sub>	99.9% trace metals basis 53-57 wt. % in diethylene glycol monobutyl ether/ethylene glycol	particle size <250 nm (DLS)	nanoparticles paste	700355-25G
Titanium(IV) oxide, mixture of rutile and anatase	TiO <sub>2</sub>	99.9% trace metals basis 33-37 wt. % in H <sub>2</sub> O	particle size <150 nm (DLS)	dispersion nanoparticles	700347-25G 700347-100G
Titanium(IV) oxide, mixture of rutile and anatase	TiO <sub>2</sub>	99.9% trace metals basis 43-47 wt. % in xylene	particle size <100 nm (DLS)	dispersion nanoparticles	700339-100G
Cerium(IV) oxide	CeO <sub>2</sub>	>99.95% trace metals basis	particle size <50 nm (BET)	nanopowder	700290-25G 700290-100G
Zirconium(IV) oxide, dispersion	ZrO <sub>2</sub>	5 wt. % in H <sub>2</sub> O	particle size <100 nm (BET)	dispersion nanoparticles	643122-100ML 643122-500ML
Zirconium(IV) oxide, dispersion	ZrO <sub>2</sub>	10 wt. % in H <sub>2</sub> O	particle size <100 nm (BET)	dispersion nanoparticles	643025-100ML
Cerium(IV) oxide, dispersion	CeO <sub>2</sub>	10 wt. % in H <sub>2</sub> O	particle size <25 nm	dispersion nanoparticles	643009-100ML 643009-250ML
Aluminum oxide	Al <sub>2</sub> O <sub>3</sub>	20 wt. % in H <sub>2</sub> O	particle size <50 nm (TEM)	liquid (suspension)	642991-100ML
Titanium(IV) oxide, rutile	TiO <sub>2</sub>	99.5% trace metals basis	particle size <100 nm diam. × L ~10 × ~40 nm	nanopowder	637262-25G 637262-100G 637262-500G
Titanium(IV) oxide, anatase	TiO <sub>2</sub>	99.7% trace metals basis	particle size <25 nm	nanopowder	637254-50G 637254-100G 637254-500G
Silicon dioxide	SiO <sub>2</sub>	99.5% trace metals basis	particle size 5 - 15 nm (TEM)	nanopowder (spherical, porous)	637246-50G 637246-250G 637246-500G
Silicon dioxide	SiO <sub>2</sub>	99.5% trace metals basis	particle size 10 - 20 nm (BET)	nanopowder	637238-50G 637238-250G 637238-500G
Titanium(IV) oxide, mixture of rutile and anatase	TiO <sub>2</sub>	99.5% trace metals basis	particle size <100 nm (BET)	nanopowder	634662-25G 634662-100G
Cerium(IV)-zirconium(IV) oxide	(CeO <sub>2</sub> ) <sub>2</sub> (ZrO <sub>2</sub> )	99.0% trace metals basis	particle size <50 nm (BET)	nanopowder	634174-25G 634174-100G
Silicon	Si	≥98% trace metals basis	particle size <100 nm (TEM)	nanopowder	633097-10G 633097-25G
Zirconium(IV) oxide	ZrO <sub>2</sub>	-	particle size <100 nm (TEM)	nanopowder	544760-5G 544760-25G
Aluminum oxide	Al <sub>2</sub> O <sub>3</sub>	-	particle size <50 nm (TEM)	nanopowder	544833-10G 544833-50G
Cerium(IV) oxide	CeO <sub>2</sub>	-	particle size <25 nm (BET)	nanopowder	544841-5G 544841-25G
Magnesium oxide	MgO	-	particle size <50 nm (BET)	nanopowder	549649-5G 549649-25G
Aluminum oxide	Al <sub>2</sub> O <sub>3</sub>	-	diam. × L 2-6 × 200-400 nm	nanowires	551643-10G 551643-50G



## Ruthenium Catalysis Precursors

For a complete list of available materials, visit [aldrich.com/periodic](http://aldrich.com/periodic).

Name	Composition	Purity	Form	Prod. No.
Ruthenium iodide	RuI <sub>3</sub>	≥99% trace metals basis	powder	734578-1G 734578-5G
Ruthenium	Ru	99.99% trace metals basis	powder	545023-1G
Ruthenium(III) chloride hydrate	RuCl <sub>3</sub> · xH <sub>2</sub> O	99.98% trace metals basis	powder and chunks	463779-1G 463779-5G
Hexaammineruthenium(II) chloride	[Ru(NH <sub>3</sub> ) <sub>6</sub> ]Cl <sub>2</sub>	≥99.9% trace metals basis	solid	303690-250MG 303690-1G 303690-5G
Ruthenium	Ru	99.9% trace metals basis	sponge	267406-1G 267406-5G
Ruthenium	Ru	99.9% trace metals basis	powder	209694-5G
Ruthenium(III) chloride hydrate	RuCl <sub>3</sub> · xH <sub>2</sub> O	-	powder and chunks	206229-1G 206229-5G 206229-25G
Pentaamminechlororuthenium(III) chloride	[Ru(NH <sub>3</sub> ) <sub>5</sub> Cl]Cl <sub>2</sub>	-	solid	289760-250MG 289760-1G 289760-5G
Ruthenium(III) nitrosyl nitrate solution	Ru(NO)(NO <sub>3</sub> ) <sub>x</sub> (OH) <sub>y</sub> , x+y=3	-	liquid	373567-25ML 373567-250ML
Ruthenium(III) nitrosyl chloride hydrate	Ru(NO)Cl <sub>3</sub> · xH <sub>2</sub> O	-	powder	409057-1G 409057-5G
Ruthenium(III) iodide hydrate	RuI <sub>3</sub> · H <sub>2</sub> O	-	powder	449253-1G

## Supported Ruthenium Catalysts

For a complete list of available materials, visit [aldrich.com/periodic](http://aldrich.com/periodic).

Name	Metal Loading	Form	Prod. No.
Ruthenium on carbon	5 wt. %	powder	206180-25G 206180-100G
Ruthenium on alumina	5 wt. %	powder, reduced, dry	439916-25G
Ruthenium on alumina	5 wt. %	powder	381152-10G
Ruthenium on alumina	0.5 wt. %	pellets	206199-50G 206199-250G
Ruthenium 5% on activated charcoal	5% Ru basis	powder	84031-1G
Ruthenium 5% on alumina	5% Ru basis	powder	84032-5G

# Ultra-high Purity Materials

Aldrich® Materials Science is pleased to offer a large selection of ultra-high purity metals, salts and oxides with purity of 99.999% or higher.

We offer over 300 metals, salts, and oxides with high trace metal purities and applications in areas including:

- Photovoltaics
- Magnetic Memory
- Phosphor Materials
- Biomedical Applications
- Nanoparticle Synthesis
- Electronic Devices



Name	Formula	Purity (Trace Metals Basis)	Aldrich Prod. No.
Europium(II) Bromide	$\text{EuBr}_2$	99.999%	<a href="#">751936</a>
Zinc Chloride	$\text{ZnCl}_2$	99.999%	<a href="#">229997</a>
Mercury	Hg	99.9999%	<a href="#">294594</a>
Aluminum(III) Fluoride	$\text{AlF}_3$	99.999%	<a href="#">752983</a>
Gallium(III) Chloride	$\text{GaCl}_3$	99.999%	<a href="#">427128</a>
Zinc Fluoride	$\text{ZnF}_2$	99.999%	<a href="#">752819</a>
Bismuth(III) Bromide	$\text{BiBr}_3$	99.999%	<a href="#">654981</a>
Germanium(IV) Oxide	$\text{GeO}_2$	99.999%	<a href="#">483001</a>
Germanium	Ge	99.999%	<a href="#">263230</a>
Tellurium	Te	99.999%	<a href="#">204544</a>
Lanthanum Oxide	$\text{La}_2\text{O}_3$	99.999%	<a href="#">203556</a>
Barium Fluoride	$\text{BaF}_2$	99.999%	<a href="#">652458</a>

Name	Formula	Purity (Trace Metals Basis)	Aldrich Prod. No.
Indium(I) Iodide	InI	99.999%	<a href="#">578606</a>
Gold	Au	99.999%	<a href="#">326542</a>
Aluminum Chloride	$\text{AlCl}_3$	99.999%	<a href="#">563919</a>
Erbium(III) Bromide	$\text{ErBr}_3$	99.999%	<a href="#">575224</a>
Holmium(III) Bromide	$\text{HoBr}_3$	99.999%	<a href="#">575232</a>
Dysprosium(III) Bromide	$\text{DyBr}_3$	99.999%	<a href="#">575240</a>
Silicon	Si	99.999%	<a href="#">267414</a>
Copper	Cu	99.9995%	<a href="#">254177</a>
Antimony(III) Oxide	$\text{Sb}_2\text{O}_3$	99.999%	<a href="#">202649</a>
Cobalt(II) Chloride	$\text{CoCl}_2$	99.999%	<a href="#">409332</a>
Lead(II) Iodide	$\text{PbI}_2$	99.999%	<a href="#">554359</a>



For a complete list of ultra-high purity products, visit [aldrich.com/uhp](http://aldrich.com/uhp)

# Changing the Landscape of Environmental and Energy Research Through Novel Nanoscale Materials



Santanu Chaudhuri  
ISP/Applied Sciences Laboratory  
Washington State University, WA 99210-1495  
chaudhuri@wsu.edu

## Introduction

Energy and environmental catalysts (EECs) form a major group of materials that will continue to drive the growth of industry and research investments. The EEC market is estimated to be between \$10–16 billion and continues to favor new systems with low operational and recycling costs. The stability of catalytic systems is highly dependent on maintaining controlled operating conditions and the ability to regenerate the catalyst bed to retain the catalytic efficiency. Many of the noble and precious metals are in low supply, and sustainable practices in catalysis are becoming more important along with the search for alternative technologies. Key regulatory developments and upcoming changes in automobile emissions will also heighten the demands on current commercial catalytic systems and push the traditional catalysts to their performance limit. Especially for the control of NO<sub>x</sub>, hydrocarbon and CO/CO<sub>2</sub> emissions under very lean burning conditions, new systems will be required for efficient vehicle technologies. For energy storage and conversion, the catalysis community is seeking game changers with novel means of turning abundant materials into active catalysts with potential regeneration pathways to extend their lifetime. From conversion of solar radiation, hydrogen storage, and fuel cell applications to improving the conversion of biofuels from different feedstocks, nanoscale catalysts with the ability to be incorporated in reactors and energy conversion/storage systems are becoming key drivers for catalysis research. It seems paramount that nanoscale materials with exceptional activity, selectivity, and stability are needed to meet these demanding performance objectives.

This article provides a perspective on important advances in nanoscale catalysis and identifies key areas needing further development. In particular, the combination of traditional synthesis and testing protocols for catalyst design will need to be augmented by precise surface science experiments and theoretical modeling of possible catalytic reaction pathways. Results of *in situ* spectroscopy on single crystal surfaces and supported catalysts are often difficult to compare with polycrystalline or supported nanoscale catalysts. A sustained effort is needed to combine promising experimental results on precise mechanisms of catalytic reactions with first-principles modeling/simulations and high-throughput screening of catalyst/support combinations. Validated experimental/modeling frameworks for material design can significantly shorten the development times for major classes of catalysts.

## Automotive and Environmental Applications

Modern vehicular and industrial operations are critically dependent on the performance of catalytic systems. Important classes of catalytic systems have made progress using nanoscale technologies in laboratory-scale research efforts. There are great opportunities for scale-up, stabilization, and reduced-cost preparation methods in such catalytic systems for technology maturation and commercial use. The current technology in catalytic conversion depends on combinations of precious metals such as Pt ([Aldrich Prod. No. 520780](#)), Pd ([Aldrich Prod. No. 267082](#)), and Rh ([Aldrich Prod. No. 204218](#)) for the reduction of CO, NO<sub>x</sub>, and hydrocarbons (HC). As an alternative to such traditional methods with platinum group metals (PGM), promising zeolite-based catalysts and transition metal-based catalysts are also explored. The promise of nanoscale catalysts is reducing the net cost of PGM in a catalyst bed due to their higher surface area and kinetics while managing challenges regarding their chemical/thermal stability. The use of ultra-small metal clusters of Pt, Pd, Au ([Aldrich Prod. No. 265772](#)), Ag ([Aldrich Prod. No. 265500](#)), and Cu has been pursued in selective catalytic reduction (SCR) research. There is also a strong correlation of reactivity with support; such as zeolites, Al<sub>2</sub>O<sub>3</sub> ([Aldrich Prod. No. 319767](#)), ZrO<sub>2</sub> ([Aldrich Prod. No. 230693](#)), MgO ([Aldrich Prod. No. 203718](#)), SiO<sub>2</sub> ([Aldrich Prod. No. 342831](#)), or TiO<sub>2</sub> ([Aldrich Prod. No. 204757](#)). For example, catalysts on aluminosilicates, such as Pt/MCM-41 ([Aldrich Prod. No. 205915](#) or [Prod. No. 643653](#)), have activity superior to a Pt/SiO<sub>2</sub> or Pt/Al<sub>2</sub>O<sub>3</sub> catalyst due to an ability to improve surface area and pore size ratios to obtain optimal performance. Pt/BaO/Al<sub>2</sub>O<sub>3</sub>-based catalysts also show high performance and high selectivity in NO<sub>x</sub>/CH<sub>4</sub> streams. Stability of small metal clusters on different supports and in the presence of other reducing agents such as CO, H<sub>2</sub>, NH<sub>3</sub>, and hydrocarbons is a challenging area for catalyst stabilization. Currently, reasonably stable Pd-Rh/BaO/CeO<sub>2</sub>-ZrO<sub>2</sub> catalysts are somewhat more economical than Pt-based catalysts. However, the search for a Pt replacement is difficult with the increasing need to reduce CO and hydrocarbons in exhaust due to tougher environmental regulations in the US and Europe. Strontium-doped perovskites (La<sub>0.9</sub>Sr<sub>0.1</sub>MnO<sub>3</sub> and La<sub>0.9</sub>Sr<sub>0.1</sub>CoO<sub>3</sub>) have shown promising performance in the SCR environment.<sup>1</sup> The partial substitution of La<sup>3+</sup> by Sr<sup>2+</sup> creates a charge imbalance that can be balanced by creation of oxygen vacancy. Although in these systems, the addition of precious metals such as Pd–Rh will still be required for hydrocarbon and CO oxidation.



## Role of Nanoarchitecture

One of the important aspects of support/nanoparticle interactions is the exposed catalyst facets and their activity on a particular support as the reactants diffuse between different exposed facets and the support. In addition, thermal stability of the nanoparticles inside of a support depends on reducing mobility of the nanoparticles using encapsulation and other immobilization methods. Examples of the use of a nanoporous support and matching architecture of support/nanoparticle components are abundant. However, many of the systems have faced challenges keeping the catalytic activities high through the thermal, adsorption/desorption cycles of impure feeds and oxidative sintering tests. As a result, use of PGM still remains high with some positive changes in the practice of reuse and a growing culture favoring sustainable use of precious metal catalysts.

### Role of Facets in Nanoparticle

For most nanoscale catalysts on oxide supports, understanding the morphology of the nanoparticles and their changes is important. Atomistic imaging techniques under realistic (non-UHV) reactive environments start to show the dynamic nature of nanoparticle surfaces due to interactions with support and reactive gas phase. Hansen et al. clearly demonstrated that the dynamic nature of faceting, shape, and size of nanoscale catalysts can be followed using atomistic imaging under realistic conditions.<sup>2</sup> Moreover, the close proximity of facets in a nanoparticle is an ideal testing ground for understanding the differences and the cooperative nature of chemistry in Pt particles, with the possibility of translating concepts from single crystal surface science studies to real catalytic materials on oxide supports.<sup>3-5</sup> For example, on platinum single crystal surfaces, the (100) surface has a higher affinity for oxygen than the (111) surface. As NO<sub>x</sub> reduction is dependent on O coverage, understanding the ratio between different facets in a nanoscale catalyst is important for understanding the balance of reactive interfaces. In fact, Komanicky et al. found that there is a “division of labor” between (111) and (100) facets in Pt nanoparticles.<sup>4</sup> The (100) nanofacet primarily supplies oxygen to the (111) for efficient reduction.

### Core/Shell Nanocatalysts

In recent developments in reducing Pt content, core/shell particles of Cu–Pt (Cu@Pt, Cu shell, Pt core and Pt@Cu Pt shell, Cu core) supported on  $\gamma$ -Al<sub>2</sub>O<sub>3</sub> have shown better NO selectivity (>90%) in the presence of H<sub>2</sub> and show promise to lower Pt content. In fact, between 250–400 °C, the Pt@Cu nanoparticles performed better than monometallic Pt.<sup>6</sup> The fundamental aspects of the near-surface alloys and the shifts in the d-band center have been described using Density Functional Theory (DFT) calculations. There are some conflicting reports in the literature about the true stability of core/shell nanostructures and all combinations of core/shell ordering are not stable under thermal cycling and repetitive reaction cycles. In reality, many core/shell structures face challenges at higher temperatures. The inter-diffusion of core/shell atoms, and the segregation of monometallic and/or stoichiometric regions are hard to control in a catalytic system.

### Mechanistic Insights on NO<sub>x</sub> Reduction

The accurate mechanism of NO<sub>x</sub> reduction is still a challenge for experimental and theoretical studies.<sup>7-9</sup> A commonly encountered 4-step Langmuir-Hinshelwood type mechanism describes the steps in the following way:

1. Adsorption:  $\text{NO} + \text{Pt} \rightarrow \text{NO-Pt}$
2. Oxygen chemisorption:  $\text{O}_2 + 2\text{Pt} \rightarrow 2\text{O-Pt}$
3. NO oxidation:  $\text{NO-Pt} + \text{O-Pt} \rightarrow \text{NO}_2\text{-Pt} + \text{Pt}$
4. Desorption:  $\text{NO}_2\text{-Pt} \rightarrow \text{NO}_2 + \text{Pt}$

### NO Reduction on Pure Metal

Optimizing the NO adsorption on a catalyst surface requires further understanding of the NO molecule and target catalyst surfaces. The first step is NO adsorbing onto Pt(111) and other low-energy terraces, steps, defects, or similar microfacets in nanoparticles. NO has three fully occupied (in mixture of 5 $\sigma$  and 1 $\pi$  orbitals) and a singly occupied electron in the antibonding 2 $\pi^*$  orbital. First-principles calculated bonding geometry and adsorption energy show a complex mixing and participation of  $\sigma$  and  $\pi^*$  orbitals with respect to Pt-d orbitals.<sup>10</sup> At high NO coverage, fcc, hcp, and atop binding sites for NO are populated in Pt-, Pd-, and Rh-based catalysts, and the ground state DFT calculations are helpful in understanding the fundamental surface chemistry and binding geometry. However, further development of kinetic theories with pressure/temperature-dependent rates, the role of spin multiplicity, and the transport of reactive species on metal surfaces for the SCR are needed to identify the full complexity and the dynamic nature of catalytic processes on PGMs at high temperatures. For example, NO and NO<sub>2</sub> are in a thermodynamic equilibrium and their sticking coefficients are surface coverage dependent. The oxygen coverage of metals and diffusion of oxygen also play an important role in determining the rate of desorption of products.

### Mechanism of NO Reduction on Supported Catalyst

The model 4-step mechanism shown (Equation 1) is not fully relevant for modern supported platinum systems with alkaline earth oxide promoters. For catalysts such as Pt/BaO/Al<sub>2</sub>O<sub>3</sub>, the BaO + NO + O<sub>2</sub> leads to nitrite species, Ba(NO<sub>2</sub>)<sub>2</sub>, which is oxidized by the Pt/O<sub>2</sub> to Ba(NO<sub>3</sub>)<sub>2</sub>, and the nitrates subsequently decompose, releasing NO<sub>2</sub>. Such processes of NO<sub>x</sub> trapping in multiphase systems is critically dependent on catalyst morphology, dispersion, and diffusion and needs careful calibration of synthesis methods to optimize performance. Beyond PGM, many base oxides/metals (e.g., Al<sub>2</sub>O<sub>3</sub>, TiO<sub>2</sub>, ZrO<sub>2</sub>, MgO promoted by Co, Ni, Cu, Fe, Sn, Ga, In, and Ag compounds) are active catalysts for the selective reduction of NO<sub>x</sub> (NO and NO<sub>2</sub>) with hydrocarbons (HC-SCR).<sup>11</sup> For zeolite- and perovskite-based catalysis, the mechanism of NO adsorption followed by desorption of N<sub>2</sub> and O<sub>2</sub> is more complex. In Cu-ZSM-5, first-principles calculations revealed the Cu-site can bind N<sub>2</sub>, O<sub>2</sub>, and NO (both mono- and di-nitrosyl) with stronger binding of NO and less strongly bound N<sub>2</sub> and O<sub>2</sub>.

## Modifying Electronic Structure of Support

Although there have been tremendous developments in synthetic techniques and a greater control of nanoparticle dispersion, size, and morphology, understanding the effect of the local electronic structure of the support remains under-utilized beyond the well-known oxide supports. It is evident that the electronic structure of the supporting oxide, its surface acidity/basicity, and the nature of its defects control the performance of a catalytic system. Once the exact mechanism and role of support is understood using first-principles modeling and experiments, many critically important aspects of the electronic structure of oxides such as MgO, Al<sub>2</sub>O<sub>3</sub>, and ZrO<sub>2</sub> can be altered using dilute transition metal and rare-earth dopants. We recently discussed the role of vacancies and oxygen chemisorption kinetics in core/shell (partially oxidized) Zr/ZrO<sub>2</sub> particles for 15 transition metal elements (Figure 1).<sup>12</sup> The role of oxide ion diffusion in the oxide matrix and trapping by impurity element doping can be utilized to improve catalyst performance. Similar efforts to change the role of the support using cationic doping of MgO by rare-earth elements showed a significant change in the defect density and the interaction with water using first-principles calculations.<sup>13</sup>

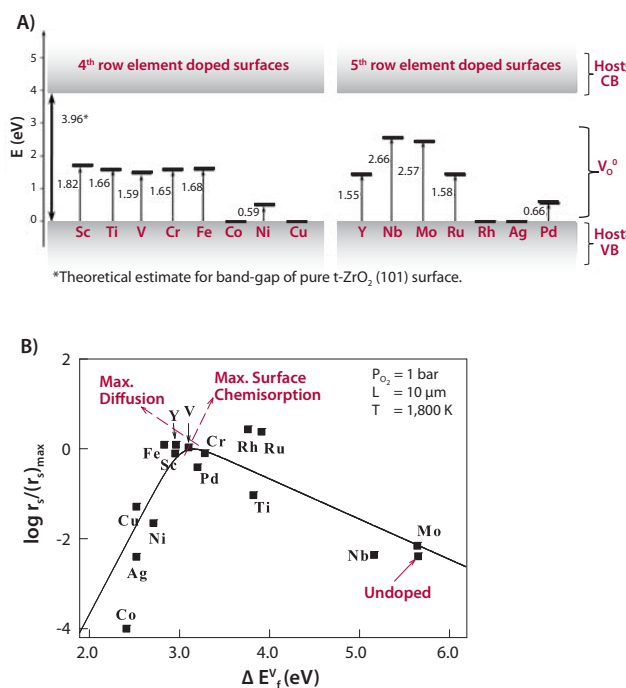


**Figure 1.** Altering the energetics and diffusion barrier in supports and high-temperature catalysts such as ZrO<sub>2</sub> can provide options of co-optimizing reactivity, defect density, and surface/bulk transport: **A)** the impurity induced changes in the defect states calculated with respect to native band gap, and **B)** volcano curve showing optimum of defect formation, oxygen chemisorption, and transport kinetic for different transition metal elements.<sup>12</sup>

## CO Oxidation on Au Catalyst

For Au nanoparticles used for CO oxidation, TiO<sub>2</sub> is the most common support. It is suggested that CO adsorbs at the edges of the Au nanoparticles and O<sub>2</sub> is actually activated around defect sites in the support. Improving defect density and accessible surface area is part of any rational approach toward improving catalytic performance. Spectroscopic studies of Au on nanocrystalline CeO<sub>2</sub> (Aldrich Prod. No. 700290) showed that CO was bonded to Au<sup>3+</sup>, Au<sup>+</sup>, and neutral Au species, whereas the active O<sub>2</sub> bonded to CeO<sub>2</sub> as superoxide η<sup>1</sup>-O<sub>2</sub>.<sup>14</sup>

From a mechanistic standpoint, DFT calculations on supported Au clusters are still a daunting task. Au is a late transition metal with 6s<sup>1</sup>4f<sup>14</sup>5d<sup>10</sup> in the valence shell and calculations need to account for relativistic effects efficiently.<sup>15</sup>

## Energy Applications

### Catalysts for Fuel Cell Research

For the fuel cell industry, the most important reaction is oxygen reduction reaction (ORR). ORR is a multielectron half-cell reaction (2O<sub>2</sub> + 2H<sup>+</sup> + 2e<sup>-</sup> = H<sub>2</sub>O) that may include a number of elementary steps involving different reaction intermediates, including inner sphere and outer sphere electron transfer mechanisms. The rate of electrocatalytic reactions such as ORR can be simplified (Equation 1) as related to the O<sub>2</sub> concentration in the solution (C<sub>O<sub>2</sub></sub>), the surface coverage of the catalyst (Pt-based catalysts) by different species (θ<sub>ad</sub>) and their change of standard free energy of adsorption (ΔG<sub>ad</sub>).

$$i = nFKC_{O_2}(1 - \theta_{ad})^x \exp\left(-\frac{\beta FE}{RT}\right), \exp\left(-\frac{\gamma \Delta G_{ad}}{RT}\right) \quad (1)$$

The current challenge is finding nanoscale materials that out-perform commercial catalysts at a lower Pt-loading level. The recent trend is to use carbon-supported binary alloys of Pt with Cr, Mn, Co, and Ni. In such bimetallic alloys, the surface structure of the stoichiometric Pt<sub>3</sub>M phase (M=Ni, Co, Fe, V, Ti) is assumed. In particular, if the d-band center of the surface electronic state of Pt<sub>3</sub>M catalyst is known from calculations or experiments, the activity of the material can be well understood.<sup>16</sup> The (1-θ<sub>ad</sub>) term in the rate expression is a rough measure of the number of O<sub>2</sub> adsorption sites available on a Pt<sub>3</sub>M catalyst surface with already-adsorbed OH from water dissociation (2H<sub>2</sub>O = OH<sub>ad</sub> + H<sub>3</sub>O<sup>+</sup> + 2e<sup>-</sup>). The preferential growth directions and shape of Pt nanoparticles also change the trends of electrocatalytic reactions. A better control of nanocatalysts dispersed on C-based support is possible if their strengths and vulnerabilities are known under controlled conditions.<sup>5</sup>

On the anode side, the fuel cell industry is plagued by the need of high-purity hydrogen with low CO content. The Pt-loading levels can be reduced using nanoscale engineering techniques and stable bimetallic catalyst surfaces. New catalysts created using novel synthetic and immobilization techniques result in increased performance and higher CO tolerance. Thus, the current trend is to identify catalysts that are capable of CO tolerances of 200 ppm and higher. Such operating conditions can be achieved in high-temperature fuel cells (HT-PEMFC) which need different nanoscale catalysts that can operate well above 100 °C and different construction of the fuel cell stacks/membrane for better water management since the Pt/C and Pt<sub>3</sub>M systems can aggregate, migrate, and reduce activity at high temperatures. As discussed in the context of NO<sub>x</sub> SCR processes, finding smarter materials for supports is critically important for low Pt-loading catalytic systems such as core/shell or bimetallic nanoscale catalysts. Novel immobilization and catalyst stabilization pathways are currently being developed to address the catalyst stability issues for HT-PEMFC.<sup>17</sup>

The energy applications for nanoscale catalysts are abundant. From photovoltaic cells to fuel cell/battery applications, the role of nanoscale catalysis in alternative energy applications is increasing. Here, we will limit our discussion to the nanoscale metal cluster catalysts in PEM fuel cells and hydrogen storage applications.



## Smaller than Nanoscale

As particle size becomes smaller, the materials research community looks at small metal clusters and identifying single-site catalysts on a support for energy and environment-related applications. The search for green fuels such as hydrogen connects environmental and energy-related catalysts in the subnanoscale to interesting domains of chemistry while blurring the lines between homogeneous and heterogeneous catalysis. The ability to isolate and manipulate the electronic structures and active molecular/atomic orbitals of individual catalytic sites is one of the promising approaches to avoid some of the stability issues of multi-phase nanoparticle-based catalysts.

## Isolated Atom-center Systems

The ability to probe chemical activity of isolated atom centers using theory and experiments is strengthening rapidly, with new applications in energy storage and conversion in mind. For example, in hydrogen storage, the search for catalysts that can activate hydrogen in ambient conditions is critically important for automobile applications. At the same time, most such systems depend on complex electrocatalytic activation and precious metals rendering them ineffective for cost-conscious automotive applications. Isolated atom centers and single-site catalysts are, therefore, sought to find catalytic centers that can act as a pump to activate hydrogen that can then subsequently be stored in a liquid or a solid for reversible use in hydrogen storage tanks. For example,  $\text{AlH}_3$  is a solid with a great potential for hydrogen storage only if catalytic centers can be found that activate hydrogen on Al allowing its use as a solid-state storage system. In our previous work, we showed using a combined theoretical and experimental approach where surfaces of abundant metals such as Al can be activated using transition-metal catalysts with metal atoms in isolation or combination, and provide a unique environment for reactions such as hydrogen activation which is otherwise impossible on Al surfaces.<sup>18</sup> This method is the first report of hydrogen activation on an Al(111) surface doped with Ti atoms at low temperatures. The unique reactive nature of surface or subsurface Ti atoms in Al is mainly due to the ability to bind and donate electrons to atomic hydrogen, leading to hydrogen chemisorption. Although theoretically predicted as a possibility, isolating Ti centers on Al supports experimentally is difficult at higher temperatures as Ti prefers subsurface and step edges in Al(111) and Al(100) surfaces. Eventually it was identified, using a combination of *in situ* surface IR spectroscopy on single crystal Al(111) doped with Ti atoms and CO as a molecular probe, that it is possible to activate hydrogen on Ti-doped Al at temperatures as low as 90 K (Figure 2).<sup>19</sup> Hydrogen storage is critically dependent on finding such cheaper alternatives to precious metals that are known to activate hydrogen at room temperature. Isolated atom-center based catalysts and single-site catalysts can also be stabilized and immobilized in a host-guest framework such as MOF or applied as a coating on electrode surfaces with greater control over nanoparticles. As such, the highest limit for dispersion of catalysts is a single catalyst on an accessible guest framework. The trajectory of catalyst development is, therefore, to design low-cost, highly dispersed catalysts with an easy regeneration route to reduce our use of precious metal catalysts in the next decade. Moreover, new catalysts are being developed to combine hydrogen storage and  $\text{CO}_2$  sequestration in a new twist to environmental catalyst and energy storage applications. For example, in a promising example from homogeneous catalysis, Ir-containing organometallic clusters have been shown to reversibly store and release  $\text{H}_2/\text{CO}_2$

at specific pH via formation of formic acid ( $\text{H}_2(\text{aq.}) + \text{CO}_2(\text{aq.}) \leftrightarrow \text{OHCOOH}(\text{aq.})$ ) from an aqueous solution.<sup>20</sup> New methods to separate the two gases in a one-step process can revolutionize hydrogen storage possibilities in a liquid.

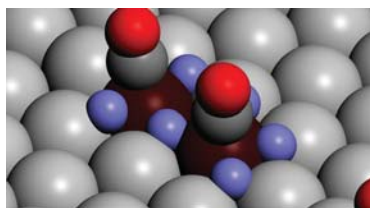


**Figure 2.** CO as a probe for identifying an isolated catalytic center: image shows an Al(111) surface with one of the Ti containing active sites. This surface can activate  $\text{H}_2$  at the surprisingly low temperature of 90 K. CO can be used to identify active sites and hydrogen spillover using the blue-shift of surface IR spectrum.<sup>19</sup>

## Conclusion

With reduction in the size of gas conversion systems for automotive and environmental applications, the trends that started with nanoscale catalysts are now being tested in single-site and isolated atom-center based catalytic systems with increasing importance. There is a growing recognition of the need to combine organic/inorganic supports with stability, selectivity, and tunable reactivity in catalytic centers. Many new methods for manipulating activity and controlling catalytic lifetime have grown in complexity, along with our growing understanding of the fundamental role of electronic structure of active sites in realistic environments using combinations of theory and experiments. This trend will continue to deliver some of the great discoveries of our time in energy and environmental applications using clever utilization of nanoscale understanding of catalytic processes.

## References

- (1) Kim, C. H.; Qi, G. S.; Dahlberg, K.; Li, W. *Science* **2010**, *327*, 1624.
- (2) Hansen, P. L.; Helveg, S.; Datye, A. K. *Adv Catal* **2006**, *50*, 77.
- (3) Yoshida, H.; Matsuura, K.; Kuwauchi, Y.; Kohno, H.; Shimada, S.; Haruta, M.; Takeda, S. *Appl Phys Express* **2011**, *4*.
- (4) Komanicky, V.; Iddir, H.; Chang, K. C.; Menzel, A.; Karapetrov, G.; Hennessy, D.; Zapol, P.; You, H. *J Am Chem Soc* **2009**, *131*, 5732.
- (5) Subhramannia, M.; Pillai, V. K. *J Mater Chem* **2008**, *18*, 5858.
- (6) Zhou, S. H.; Varughese, B.; Eichhorn, B.; Jackson, G.; Mcllwraith, K. *Angew Chem Int Edit* **2005**, *44*, 4539.
- (7) Liu, G.; Gao, P. X. *Catal Sci Technol* **2011**, *1*, 552.
- (8) Bowker, M. *Chem Soc Rev* **2008**, *37*, 2204.
- (9) Broqvist, P.; Gronbeck, H.; Fridell, E.; Panas, I. *Catal Today* **2004**, *96*, 71.
- (10) Getman, R. B.; Schneider, W. F. *J Phys Chem C* **2007**, *111*, 389.
- (11) Burch, R.; Breen, J. P.; Meunier, F. C. *Appl Catal B-Environ* **2002**, *39*, 283.
- (12) Kwak, H.; Chaudhuri, S. *Surf Sci* **2010**, *604*, 2116.
- (13) Kwak, H.; Chaudhuri, S. *J Alloy Compd* **2011**, *509*, 8189.
- (14) Guzman, C.; Del Angel, G.; Gomez, R.; Galindo, F.; Zanella, R.; Torres, G.; Angeles-Chavez, C.; Fierro, J. L. G. *J Nano Res-Sw* **2009**, *5*, 13.
- (15) Coquet, R.; Howard, K. L.; Willock, D. J. *Chem Soc Rev* **2008**, *37*, 2046.
- (16) Stamenkovic, V. R.; Mun, B. S.; Arenz, M.; Mayrhofer, K. J. J.; Lucas, C. A.; Wang, G. F.; Ross, P. N.; Markovic, N. M. *Nat Mater* **2007**, *6*, 241.
- (17) Chevallier, L.; Bauer, A.; Cavaliere, S.; Hui, R.; Roziere, J.; Jones, D. J. *ACS Appl Mater Inter* **2012**, *4*, 1752.
- (18) Chaudhuri, S.; Graetz, J.; Ignatov, A.; Reilly, J. J.; Muckerman, J. T. *J Am Chem Soc* **2006**, *128*, 11404.
- (19) Chopra, I. S.; Chaudhuri, S.; Veyan, J. F.; Chabal, Y. J. *Nat Mater* **2011**, *10*, 884.
- (20) Hull, J. F.; Himeda, Y.; Wang, W. H.; Hashiguchi, B.; Periana, R.; Szalda, D. J.; Muckerman, J. T.; Fujita, E. *Nat Chem* **2012**, *4*, 383.

## Noble Metal Catalysts

For a complete list of available materials, visit [aldrich.com/metals](http://aldrich.com/metals).

Name	Composition	Purity	Form	Prod. No.
Palladium	Pd	≥99.5% trace metals basis	nanopowder	686468-500MG
Platinum black	Pt	≥99.9% trace metals basis	powder	520780-1G 520780-5G
Palladium	Pd	99.9% trace metals basis	powder	464651-5G 464651-25G
Platinum	Pt	99.9% trace metals basis	powder	327476-500MG 327476-5G
Platinum	Pt	≥99.9% trace metals basis	powder	327441-500MG 327441-5G
Palladium	Pd	≥99.9% trace metals basis	powder	326666-1G 326666-5G
Rhodium	Rh	99.9% trace metals basis	sponge	267368-250MG 267368-1G
Platinum	Pt	≥99.9% trace metals basis	sponge	267155-1G 267155-5G
Palladium	Pd	99.9% trace metals basis	sponge	267082-1G 267082-5G
Rhodium	Rh	99.95% trace metals basis	powder	204218-1G
Platinum	Pt	-	nanopowder	685453-250MG

## Mesoporous Materials for Catalyst Supports

For a complete list of available materials, visit [aldrich.com/mesoporous](http://aldrich.com/mesoporous).

Name	Composition	Dimensions	Form	Prod. No.
Carbon, mesoporous	C	particle size distribution 45 μm ±5 average pore diameter 100 Å ±10 Å (typical) pore volume 0.5 cm <sup>3</sup> /g (typical)	powder	699640-5G 699640-25G
Carbon, mesoporous	C	mesoporosity 0.4-0.7 cm <sup>3</sup> /g microporosity 0-0.2 cm <sup>3</sup> /g	powder	702102-5G
Carbon, mesoporous	C	mesoporosity > 0.2 cm <sup>3</sup> /g	powder	702110-5G
Carbon, mesoporous	C	particle size <500 nm (DLS) average pore diameter 64 Å (typical) total pore volume 0.342 cm <sup>3</sup> /g (typical)	nanopowder	699632-5G 699632-25G
Aluminosilicate, mesostructured	(SiO <sub>2</sub> ) <sub>x</sub> (Al <sub>2</sub> O <sub>3</sub> ) <sub>y</sub>	pore size 2.5-3 nm pore volume 1.0 cm <sup>3</sup> /g	powder	643653-5G 643653-25G
Silica, mesostructured	SiO <sub>2</sub>	pore size 2.1-2.7 nm pore volume 0.98 cm <sup>3</sup> /g	powder	643645-5G 643645-25G
Silica, mesostructured	SiO <sub>2</sub>	pore size ~ 7.1 nm pore volume 0.91 cm <sup>3</sup> /g	powder	643637-5G 643637-25G
Aluminosilicate, mesostructured	(SiO <sub>2</sub> ) <sub>x</sub> (Al <sub>2</sub> O <sub>3</sub> ) <sub>y</sub>	pore volume 2.03 cm <sup>3</sup> /g	powder	643629-5G 643629-25G
Silica, mesostructured	SiO <sub>2</sub>	pore volume 2.31 cm <sup>3</sup> /g	powder	560979-10G
Silica, mesostructured	SiO <sub>2</sub>	particle size 3.05 μm (avg.) pore size 3.9 nm (avg.) pore volume 1.76 cm <sup>3</sup> /g	powder	541036-5G 541036-25G
Aluminum oxide, mesoporous	Al <sub>2</sub> O <sub>3</sub>	particle size 4.4 μm (avg.) pore size 6.5 nm	powder	517755-5G
Aluminum oxide, mesoporous	Al <sub>2</sub> O <sub>3</sub>	particle size 5.65 μm (avg.) average pore size 3.8 nm	powder	517747-5G

## Noble Metal Precursors

For a complete list of available materials, visit [aldrich.com/periodic](http://aldrich.com/periodic).

Name	Composition	Purity	Form	Prod. No.
Palladium(II) nitrate dihydrate	$\text{Pd}(\text{NO}_3)_2 \cdot 2\text{H}_2\text{O}$	~40% Pd basis	powder or crystals	76070-1G 76070-5G
Palladium(II) acetate, recrystallized	$\text{Pd}(\text{OCOCH}_3)_2$	97%	powder	720070-1G
Platinum(IV) chloride	$\text{PtCl}_4$	≥99.9% trace metals basis	powder	520640-1G 520640-5G
Platinum(II) chloride	$\text{PtCl}_2$	≥99.9%	powder	520632-1G 520632-5G
Platinum(II) chloride	$\text{PtCl}_2$	≥99.99% trace metals basis	powder	482315-1G
Rhodium(III) chloride hydrate	$\text{RhCl}_3 \cdot x\text{H}_2\text{O}$	99.98% trace metals basis	crystalline	450286-250MG 450286-1G
Platinum(IV) chloride	$\text{PtCl}_4$	≥99.99% trace metals basis	powder and chunks	379840-250MG 379840-1G
Tetraamminepalladium(II) chloride monohydrate	$\text{Pd}(\text{NH}_3)_4\text{Cl}_2 \cdot \text{H}_2\text{O}$	≥99.99% trace metals basis	powder or crystals	323438-1G 323438-5G
Rhodium(III) chloride	$\text{RhCl}_3$	98%	crystalline	307866-500MG 307866-2.5G
Platinum(IV) chloride	$\text{PtCl}_4$	96%	powder and chunks	206113-250MG 206113-1G 206113-5G
Palladium(II) chloride	$\text{Cl}_2\text{Pd}$	99%	powder	205885-1G 205885-5G 205885-25G 205885-150G
Palladium(II) nitrate hydrate	$\text{Pd}(\text{NO}_3)_2 \cdot x\text{H}_2\text{O}$	-	powder and chunks	205761-2G 205761-10G
Rhodium(III) chloride hydrate	$\text{RhCl}_3 \cdot x\text{H}_2\text{O}$	-	powder or crystals	206261-250MG 206261-1G 206261-5G 206261-10G 206261-25G

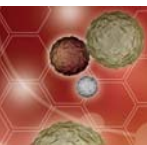
## Catalyst Supports

For a complete list of available materials, visit [aldrich.com/periodic](http://aldrich.com/periodic).

Name	Composition	Purity	Form	Prod. No.
Magnesium oxide	$\text{MgO}$	99.995% trace metals basis	powder	529699-10G 529699-50G
Cerium(IV) oxide	$\text{CeO}_2$	99.9% trace metals basis	fused (pieces)	342955-50G
Silicon dioxide	$\text{SiO}_2$	99.5% trace metals basis	powder	342890-100G 342890-1KG
Silicon dioxide	$\text{SiO}_2$	99.99% trace metals basis	fused (pieces)	342858-25G
Silicon dioxide	$\text{SiO}_2$	99.9% trace metals basis	fused (granular)	342831-100G 342831-1KG
Barium oxide	$\text{BaO}$	97%	powder	288497-50G 288497-250G
Titanium(IV) oxide, anatase	$\text{TiO}_2$	≥99% trace metals basis	powder	248576-100G 248576-1KG 248576-10KG
Titanium(IV) oxide, anatase	$\text{TiO}_2$	99.8% trace metals basis	powder	232033-100G 232033-500G
Titanium(IV) oxide, rutile	$\text{TiO}_2$	≥99.9% trace metals basis	powder	224227-5G 224227-100G 224227-500G
Cerium(IV) oxide	$\text{CeO}_2$	99.9% trace metals basis	powder	211575-100G 211575-500G
Titanium(IV) oxide, rutile	$\text{TiO}_2$	99.99% trace metals basis	powder	204757-25G 204757-125G
Magnesium oxide	$\text{MgO}$	99.99% trace metals basis	powder	203718-5G 203718-25G 203718-100G
Cerium(IV) oxide	$\text{CeO}_2$	99.995% trace metals basis	powder	202975-10G 202975-50G



Changing the Landscape of Environmental and Energy Research Through Novel Nanoscale Materials



## Supported Platinum Catalysts

For a complete list of available materials, visit [aldrich.com/renewable](http://aldrich.com/renewable).

Name	Metal Loading	Form	Prod. No.
Platinum on graphitized carbon	10 wt. %	powder	738581-1G
Platinum on graphitized carbon	20 wt. %	powder	738549-1G
Platinum-ruthenium alloy on graphitized carbon	Pt 20 wt. % Ru 10 wt. %	powder	738573-1G
Platinum cobalt on carbon	Pt <sub>3</sub> Co 30 wt. %	powder	738565-1G
Platinum on graphitized carbon	40 wt. %	powder	738557-1G
Platinum on silica	1 wt. %	dry granular	520691-25G 520691-100G
Platinum on carbon	1 wt. %	powder	205923-5G 205923-25G

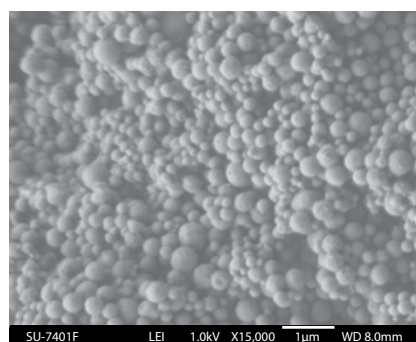
## Catalyst Precursors

For a complete list of available materials, visit [aldrich.com/periodic](http://aldrich.com/periodic).

Name	Composition	Purity	Form	Prod. No.
Nickel carbonate, basic hydrate	NiCO <sub>3</sub> · 2Ni(OH) <sub>2</sub> · xH <sub>2</sub> O	99.9%, trace metals analysis 99.9% trace metals basis	powder	544183-250G-A 544183-1KG-A
Copper(II) acetylacetonate	Cu(C <sub>5</sub> H <sub>7</sub> O <sub>2</sub> ) <sub>2</sub>	≥99.99% trace metals basis	powder	514365-10G 514365-50G
Cobalt(III) acetylacetonate	Co(C <sub>5</sub> H <sub>7</sub> O <sub>2</sub> ) <sub>3</sub>	99.99% trace metals basis	granular powder or crystals	494534-5G 494534-25G
Copper(II) nitrate hemi(pentahydrate)	Cu(NO <sub>3</sub> ) <sub>2</sub> · 2.5H <sub>2</sub> O	≥99.99% trace metals basis	crystalline	467855-50G 467855-250G
Nickel(II) oxalate dihydrate	NiC <sub>2</sub> O <sub>4</sub> · 2H <sub>2</sub> O	99.999% trace metals basis	powder	463787-10G
Copper(II) chloride	CuCl <sub>2</sub>	≥99.995% trace metals basis	powder	451665-5G 451665-25G
Nickel(II) chloride	NiCl <sub>2</sub>	99.99% trace metals basis	powder	451193-5G 451193-25G
Cobalt(II) chloride	CoCl <sub>2</sub>	99.9% trace metals basis	beads	449776-5G 449776-25G
Cobalt(II) acetate tetrahydrate	(CH <sub>3</sub> COO) <sub>2</sub> Co · 4H <sub>2</sub> O	99.999% trace metals basis	powder and chunks	437875-1G 437875-10G
Cobalt(II) chloride	CoCl <sub>2</sub>	99.999% trace metals basis	beads	409332-1G 409332-5G
Copper(II) formate hydrate	(HCO <sub>2</sub> ) <sub>2</sub> Cu · xH <sub>2</sub> O	97%	powder	404942-50G
Copper(I) acetate	CuCO <sub>2</sub> CH <sub>3</sub>	97%	powder and chunks	403342-1G 403342-10G
Cobalt(II) acetate	(CH <sub>3</sub> CO <sub>2</sub> ) <sub>2</sub> Co	99.995% trace metals basis	crystals and lumps	399973-1G 399973-10G
Cobalt(II) carbonate hydrate	CoCO <sub>3</sub> · xH <sub>2</sub> O	99.998% trace metals basis	powder	379956-5G
Nickel(II) acetate tetrahydrate	Ni(OCOCH <sub>3</sub> ) <sub>2</sub> · 4H <sub>2</sub> O	99.998% trace metals basis	powder and chunks	379883-10G 379883-50G
Cobalt(II) hydroxide	Co(OH) <sub>2</sub>	95%	powder	342440-250G
Cobalt(II) hexafluoroacetylacetonate hydrate	Co(C <sub>5</sub> HF <sub>6</sub> O <sub>2</sub> ) <sub>2</sub> · xH <sub>2</sub> O	98%	powder or crystals	339695-5G
Copper(II) nitrate hydrate	Cu(NO <sub>3</sub> ) <sub>2</sub> · xH <sub>2</sub> O	99.999% trace metals basis	crystals and lumps	229636-5G 229636-25G 229636-100G
Copper(II) perchlorate hexahydrate	Cu(ClO <sub>4</sub> ) <sub>2</sub> · 6H <sub>2</sub> O	98%	crystalline	215392-5G 215392-100G
Nickel(II) nitrate hexahydrate	Ni(NO <sub>3</sub> ) <sub>2</sub> · 6H <sub>2</sub> O	99.999% trace metals basis	solid	203874-20G 203874-100G 203874-500G
Cobalt(II) nitrate hexahydrate	Co(NO <sub>3</sub> ) <sub>2</sub> · 6H <sub>2</sub> O	99.999% trace metals basis	crystals and lumps	203106-10G 203106-50G

# Functionalized Nanoporous Silica

Aldrich® Materials Science offers a wide range of porous materials including nanoporous silica, nanoporous alumina, and functional nanoporous silica materials for biomedical applications. Fluorescent-labeled nanoporous silica particles aimed at diagnostics are a new range of tailored nanoporous products also offered.



Product Name	Particle Size	Pore Size	Wavelength ( $\lambda_{ex}/\lambda_{em}$ )	Description	Aldrich Prod. No.
Propylamine Functionalized Nanoporous Silica particles	<100 nm	4 nm	N/A	Surface functional group: Propylamine ( $-C_3H_7NH_2$ )	749265
Propylthiol Functionalized Nanoporous Silica	<100 nm	4 nm	N/A	Surface functional group: Propylthiol ( $-C_3H_7SH$ )	749362
Propylcarboxylic Acid Functionalized Nanoporous Silica Particles	<100 nm	4 nm	N/A	Surface functional group: Propylcarboxylic Acid ( $-C_3H_7COOH$ )	749664
Propylcarboxylic Acid Functionalized Porphine-labeled Nanoporous Silica Particles	<100 nm	4 nm	416/670 nm	Surface functional group: Propylcarboxylic Acid ( $-C_3H_7COOH$ ) Fluorescent loaded : meso-Tetra(4-carboxyphenyl) porphine(TCPP)	749680
Propylcarboxylic Acid Functionalized Fluorescein-labeled Nanoporous Silica particles	<100 nm	4 nm	488/520 nm	Surface functional group: Propylcarboxylic Acid ( $-C_3H_7COOH$ ) Fluorescent loaded : Fluorescein isothiocyanate (FITC)	749699
Propylthiol Functionalized Fluorescein-labeled Nanoporous Silica particles	<100 nm	5 nm	488/520 nm	Surface functional group: Thiol Functional groups, ( $-C_3H_7SH$ ) Fluorescent loaded : Fluorescein isothiocyanate (FITC)	749702
Propylthiol Functionalized Porphine-labeled Nanoporous Silica	<100 nm	4 nm	416/670 nm	Surface functional group: Thiol Functional groups, ( $-C_3H_7SH$ ) Fluorescent loaded : meso-Tetra(4-carboxyphenyl) porphine(TCPP)	749710

For a complete list of mesoporous materials, visit [aldrich.com/mesoporous](http://aldrich.com/mesoporous)



# MOF Constructor Tool

## Building Frameworks for Your Research

**Metal-Organic Frameworks (MOFs)** are a novel class of porous 3D-networked, crystalline materials composed of metal ions or clusters connected by organic linkers, and are designed for applications requiring high surface areas.

The MOF Constructor Tool from Aldrich® Materials Science offers easy access to our portfolio of organic linkers and metal precursors including inorganic secondary building units (SBUs) suitable for the preparation of MOFs.

To use our MOF Constructor Tool and find the materials for your MOF research by refining the building units (Organic Linker or Metal Source) as well as MOF name, Applications and Surface Area, visit [aldrich.com/mofconstructor](http://aldrich.com/mofconstructor).

**Build your framework:** Linker Metal Source

**Filter by:** Application Surface Area (m<sup>2</sup>/g)

**Locate a specific MOF:** MOF [RESET FILTERS >](#) [SHOW ALL MOFS >](#)

MOF Name	Linker	Metal Source	Application	Surface Area (m <sup>2</sup> /g)
Al(OH)(BDC)	TPA, H <sub>2</sub> BDC, BDC Terephthalic acid (185361)	Al	Catalysis (Isomerization of $\alpha$ -pinene oxide)	950 (BET Surface Area)
Al-MIL-53-X	H <sub>4</sub> DOBDC 2,5-Dihydroxyterephthalic acid (382132)	Al	Gas Adsorption	
BCF-1	TMA, H <sub>3</sub> BTC, BTC Trimesic acid (482749)	Be		

[MORE INFO >](#)



For more information, visit  
[aldrich.com/mofconstructor](http://aldrich.com/mofconstructor)